CrossMark

The Transmission Spectrum of WASP-17 b From the Optical to the Near-infrared Wavelengths: Combining STIS, WFC3, and IRAC Data Sets

Arianna Saba[1] , Angelos Tsiaras[1,2] , Mario Morvan[1] , Alexandra Thompson[1] , Quentin Changeat[1] , Billy Edwards[1,3] , Andrew Jolly[4] , Ingo Waldmann[1] , and Giovanna Tinetti[1]

[1] Department of Physics and Astronomy, University College London, Gower Street, WC1E 6BT London, UK; arianna.saba.20@ucl.ac.uk
[2] INAF—Osservatorio Astrofisico di Arcetri, Largo E. Fermi 5, I-50125 Firenze, Italy
[3] AIM, CEA, CNRS, Université Paris-Saclay, Université de Paris, F-91191 Gif-sur-Yvette, France
[4] School of Physics, University of New South Wales, Sydney, NSW 2052, Australia

Abstract

We present the transmission spectrum of the inflated hot Jupiter WASP-17 b, observed with the STIS and WFC3 instruments aboard the Hubble Space Telescope, allowing for a continuous wavelength coverage from ∼0.4 to ∼1.7 μm. Observations taken with IRAC channels 1 and 2 on the Spitzer Space Telescope are also included, adding photometric measurements at 3.6 and 4.5 μm. HST spectral data were analyzed with Iraclis, a pipeline specialized in the reduction of STIS and WFC3 transit and eclipse observations. Spitzer photometric observations were reduced with the TLCD-LSTM method, utilizing recurrent neural networks. The outcome of our reduction produces incompatible results between STIS visit 1 and visit 2, which leads us to consider two scenarios for G430L. Additionally, by modeling the WFC3 data alone, we can extract atmospheric information without having to deal with the contrasting STIS data sets. We run separate retrievals on the three spectral scenarios with the aid of TauREx 3, a fully Bayesian retrieval framework. We find that, independently of the data considered, the exoplanet atmosphere displays strong water signatures and, potentially, the presence of aluminum oxide and titanium hydride. A retrieval that includes an extreme photospheric activity of the host star is the preferred model, but we recognize that such a scenario is unlikely for an F6-type star. Due to the incompleteness of all STIS spectral light curves, only further observations with this instrument would allow us to properly constrain the atmospheric limb of WASP-17 b, before the James Webb Space Telescope or Ariel will come online.

1. Introduction

In recent years, the Hubble Space Telescope (HST) has been at the forefront of exoplanet atmospheric characterization. Thanks to its Wide Field Camera 3 (WFC3) and its Space Telescope Imaging Spectrograph (STIS), often combined with the InfraRed Array Camera (IRAC) aboard the Spitzer Space Telescope, the atmospheres of hot Jupiters (Sing et al. 2016; Pinhas et al. 2018; Tsiaras et al. 2018; Pluriel et al. 2020a; Skaf et al. 2020), ultrahot Jupiters (Kreidberg et al. 2018; Mikal-Evans et al. 2019; Changeat et al. 2020; Edwards et al. 2020a), super-Earths (Tsiaras et al. 2016a, 2019; Edwards et al. 2020b; Mugnai et al. 2021), sub-Neptunes (Guilluy et al. 2020; Guo et al. 2020), and hot Saturns (Anisman et al. 2020; Carone et al. 2021) have been studied in transmission, in emission, and across their phase curves (Knutson et al. 2012; Stevenson et al. 2017; Kreidberg et al. 2018; Arcangeli et al. 2019; Feng et al. 2020; Irwin et al. 2020; Changeat et al. 2021). Although small rocky planets are difficult to probe with current spectrographs owing to the limited signal-to-noise ratio (S/N) of their gaseous envelope, atmospheric studies conducted on extrasolar gas giants reported the detection of various molecules, in particular water vapor.

Among the exoplanet population of inflated hot Jupiters, WASP-17 b (Anderson et al. 2010) is one of the least dense

planets discovered so far, with a radius equal to 1.932 ± 0.053 R_J and a mass 0.477 times that of Jupiter (Southworth et al. 2012). The transiting planet, confirmed to possess a retrograde orbit (Bayliss et al. 2010; Hébrard et al. 2011; Simpson et al. 2011), forms an angle of $148°.5^{+5.1}_{-4.2}$ with respect to the rotation axis of its parent star (Triaud et al. 2010). The considerable orbital obliquity of WASP-17 b cannot be explained by inward migration (Lin et al. 1996; Ida & Lin 2004) but could rather be due to an initial misalignment between the star and the protoplanetary disk (Bate et al. 2010), planet–planet scattering, or the Kozai mechanism (Nagasawa et al. 2008). These processes also induce the very small eccentricities reported in orbitally misaligned planets (Johnson et al. 2009; Winn et al. 2009; Bourrier et al. 2018); in fact, Southworth et al. (2012) were not able to find any evidence of the orbital eccentricity of WASP-17 b. The exoplanet takes 3.7 days to orbit its host star (Southworth et al. 2012), an F6-type star with $V_{mag} = 11.6$ (Anderson et al. 2010).

Given the planet's very large atmospheric scale height (Anderson et al. 2010), transmission spectroscopy studies have been extremely successful. From the ground, sodium was detected at optical wavelengths by Wood et al. (2011) and Zhou & Bayliss (2012) using the Very Large Telescope (VLT) and by Khalafinejad et al. (2018) with the Magellan Telescope. At low resolution, the spectrograph FORS2 mounted on the VLT detected potassium in the atmosphere of WASP-17 b with a 3σ significance and water absorption (Sedaghati et al. 2016). From space, data taken with HST in the optical and near-infrared and with Spitzer at 3.6 and 4.5 μm report water

absorption and alkali features, with little to no clouds/hazes (Sing et al. 2016). A more recent atmospheric study on WASP-17 b (Alderson et al. 2022) further confirms the presence of H_2O in addition to CO_2 absorption in the infrared. Lastly, the study conducted by Barstow et al. (2016) reports the presence of water at solar abundances in the limb of WASP-17 b, possibly accompanied by CO signatures. However, contrary to the results by Sing et al. (2016), their best atmospheric model includes scattering aerosols at relatively high altitudes, up to 1 mbar.

Here we present the spectroscopic analysis performed on transit observations taken with STIS (gratings G430L and G750L) and WFC3 (grisms G102 and G141) on board HST and with IRAC channels 1 and 2 of the Spitzer Space Telescope. The combination of the aforementioned instruments allows us to investigate the spectrum of WASP-17 b from the optical to the near-infrared wavelengths (0.4–5 μm).

2. Methodology

2.1. HST Data Processing

2.1.1. WFC3

We downloaded the HST/WFC3 raw spectroscopic and spatially scanned observations of WASP-17 b from the Mikulski Archive for Space Telescopes (MAST), as part of the HST Proposal 14918 (P.I. Hannah Wakeford). In our study we decided to not include the HST/WFC3 data set from proposal 12181, obtained in staring mode, because of its low S/N. The data would produce error bars 6–7 times bigger compared to the other WFC3 observations, obtained in spatial scanning mode.

Two transits of the exoplanet were observed with the grisms G102 and G141, which cover wavelengths in the ranges of 0.8–1.1 μm and 1.1–1.7 μm, respectively. We employed Iraclis (Tsiaras et al. 2016b), an open-source reduction pipeline for WFC3,[5] to reduce the data and extract the light curves by performing the following steps: zero-read subtraction, reference pixels correction, nonlinearity correction, dark current subtraction, gain conversion, sky background subtraction, calibration, flat-field correction, bad-pixel and cosmic-ray correction, and light-curve extraction.

The WFC3 detector induces two different time-dependent systematics to the light curve: one exponential, at the beginning of each HST orbit, and one linear throughout the visit. Iraclis corrects for these systematics by fitting a transit fit model $F(t)$, computed using Pylightcurve, on the white light curve. $F(t)$ is a function of the limb-darkening coefficients, R_p/R_*, and the orbital parameters T_0, P, i, a/R_*, e, ω. The transit fit function is then multiplied by a normalization factor n_w and a function $R(t)$ containing a linear and an exponential term as follows:

$$R(t) = (1 - r_a(t - T_0))(1 - r_{b1}e^{-r_{b2}(t-t_0)}). \quad (1)$$

Here t is time, T_0 is the mid-transit time, t_0 is the time when each orbit starts, r_a is the slope of the linear term, and (r_{b1}, r_{b2}) are the coefficients of the exponential ramp. The spectral light curves are first fitted using Equation (1). Then, they are divided by the white light curve and further fitted via

$$n_\lambda(1 + \chi_\lambda(t - T_0))(F(\lambda, t)/F_w(t)), \quad (2)$$

---

[5] https://github.com/ucl-exoplanets/Iraclis

Stellar and Planetary Parameters	Value
T_* (K)	6550 ± 80[a]
R_* ($R_\odot$)	1.572 ± 0.056[a]
M_* ($M_\odot$)	1.306 ± 0.026[a]
$\log_{10}(g)$ (cm s^{-2})	4.161 ± 0.026[a]
[Fe/H]	-0.19 ± 0.09[a]
a/R_*	$7.27^{+0.21}_{-0.44}$
e	0 (fixed)
i (deg)	$87.96^{+1.34}_{-1.56}$
ω	0 (fixed)
P (days)	$3.7354845 \pm 1.9 \times 10^{-6}$[b]
T_0 (BJD$_{\mathrm{TDB}}$)	$2,454,592.8015 \pm 0.0005$[b]
R_p/R_*	$0.12229^{+0.00017}_{-0.00013}$
M_p (M_J)	0.477 ± 0.033[b]
R_p (R_J)	1.932 ± 0.053[b]

Notes.
[a] Anderson et al. (2011).
[b] Southworth et al. (2012).

where n_λ is a wavelength-dependent normalization factor, χ_λ is the coefficient of the wavelength-dependent linear slope, t is time, T_0 is the mid-transit time, $F(\lambda, t)$ is the wavelength-dependent transit model, and $F_w(t)$ is the best-fit model on the white light curve.

Further information on Iraclis can be found in Tsiaras et al. (2016a, 2016b, 2018).

2.1.2. STIS

We downloaded the HST/STIS raw spectroscopic observations of WASP-17 b from the Mikulski Archive for Space Telescopes (MAST), as part of the HST Proposal 12473 (P.I. David Sing).

Three transits of the exoplanet were observed with the gratings G430L (two transits) and G750L (one transit), which cover wavelengths in the ranges of 0.3–0.57 μm and 0.5–0.94 μm, respectively. For the analysis of these data sets we used again Iraclis but adapted most of the reduction steps to STIS. These steps are bias level subtraction, bias correction, image subtraction, dark image subtraction, flat-field correction, calibration, background subtraction, bad-pixel and cosmic-ray correction, and light-curve extraction. The first five steps were performed following the recipes described in the STIS Handbook (Bostroem & Proffitt 2011), while the rest were implemented in the same way as for the WFC3 staring-mode observations. For the extraction we used 6-pixel-wide apertures along the cross-dispersion direction and smoothed aperture edges along the dispersion direction (the smoothing factors were 5 Å for the G430L grating and 10 Å for the G750L grating, corresponding to approximately 2 pixels in each case).

2.2. HST Light-curve Modeling

Table 1 summarizes the parameters used for the light-curve modeling. For these parameters we consulted the Exoplanet Characterisation Catalogue developed as part of the ExoClock project (Kokori et al. 2021). In all the light-curve modeling steps we assumed a circular orbit and a fixed period for the planet, while the limb-darkening effect was modeled using the Claret
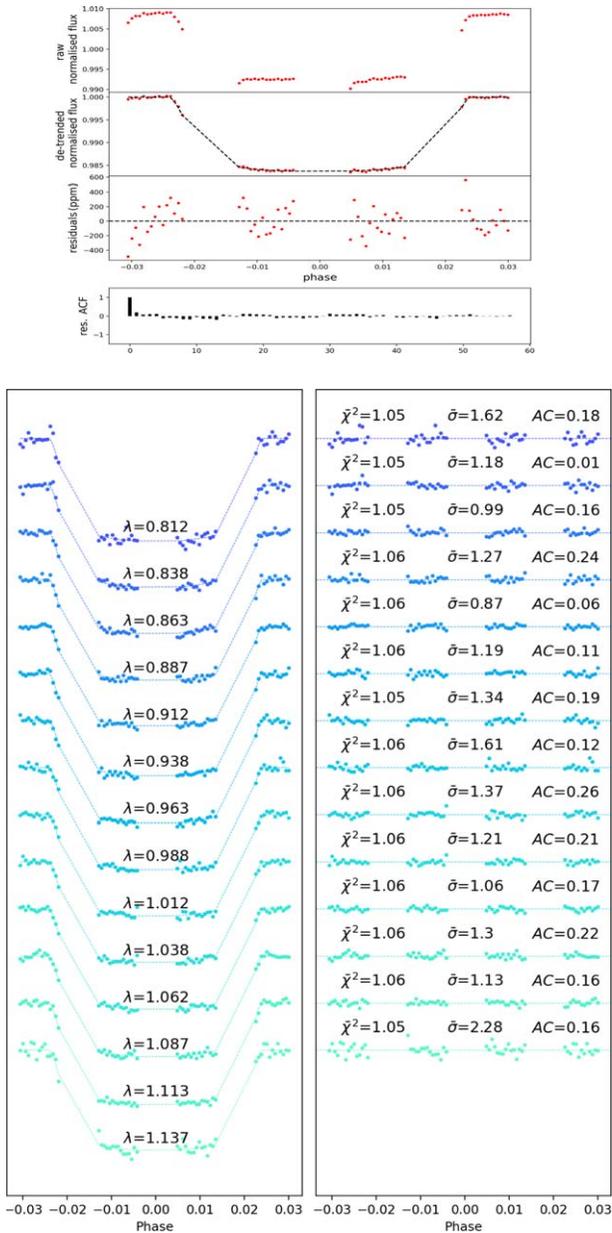
Figure 1. Top: white light curve for the HST/WFC3 G102 transmission observations of WASP-17 b. First panel: raw light curve, after normalization. Second panel: light curve, divided by the best-fit model for the systematics. Third panel: residuals for the best-fit model. Fourth panel: autocorrelation function of the residuals. Bottom: spectral light curves fitted with Iraclis for the HST/WFC3 G102 transmission spectra, where, for clarity, an offset has been applied. Left panel: the detrended spectral light curves with the best-fit model plotted. Right panel: fitting residuals with values for the χ^2, the standard deviation of the residuals with respect to the photon noise ($\bar{\sigma}$), and the autocorrelation (AC) of the residuals.

4-coefficient law (Claret [2000](#)) and the ExoTETHyS (Morello et al. [2020](#)) package, which takes into account the stellar parameters (Table [1](#)) and the response curve of the instrument.

At a first stage, the initial orbit of each HST visit was discarded since it presents more significant wavelength-dependent systematics compared to the subsequent orbits. We then analyzed only the white light curves (broad band) and left the semimajor axis, the inclination, the mid-transit time, and the R_p/R_* as free parameters, together with a number of parameters for the systematics implemented in Iraclis.

To ensure consistency between the analysis of the different data sets, we estimated again the inclination and the semimajor axis of the planet using all the available data. We combined the light curves extracted from the five HST observations, together with five TESS (Ricker et al. [2014](#)) observations. The updated parameters are reported in Table [1](#).

Finally, we analyzed all the white and spectral HST light curves, fixing the values for the semimajor axis and the inclination. Figures [1](#), [2](#), [3](#), [4](#), and [5](#) show the fitted white and spectral light curves for all the HST observations, while Tables [4](#) and [5](#) in Appendix [A](#) report the transmission data for STIS and WFC3, respectively.

2.3. Spitzer Data Analysis

Spitzer data are available on the IRSA online archive. We downloaded the WASP-17 b transit observations taken with IRAC channels 1 and 2 in 2013 (P.I. Jean–Michel Desert, program 90092). The two observations were analyzed separately by employing the light-curve detrending method named TLCD-LSTM[6] developed by Morvan et al. ([2020](#)). This approach uses a long short-term memory network (Hochreiter & Schmidhuber [1997](#)) to predict the transit light curve without the need for any prior assumptions on the noise or transit shape. The only assumption regarding the systematics is that the associated correlated noise can be inferred from the out-of-transit light curve and the centroid time series. First, photometric light curves are extracted by using a circular aperture around the center of light. We tested a grid of radius apertures ranging from 2 to 4 pixels, by increments of 0.25 pixels. We then selected the aperture that maximized the S/N, i.e., 3.25 pixels. We subtracted the background light computed at each time step using the median flux in each image after excluding a disk of radius 15 pixels around the source center.
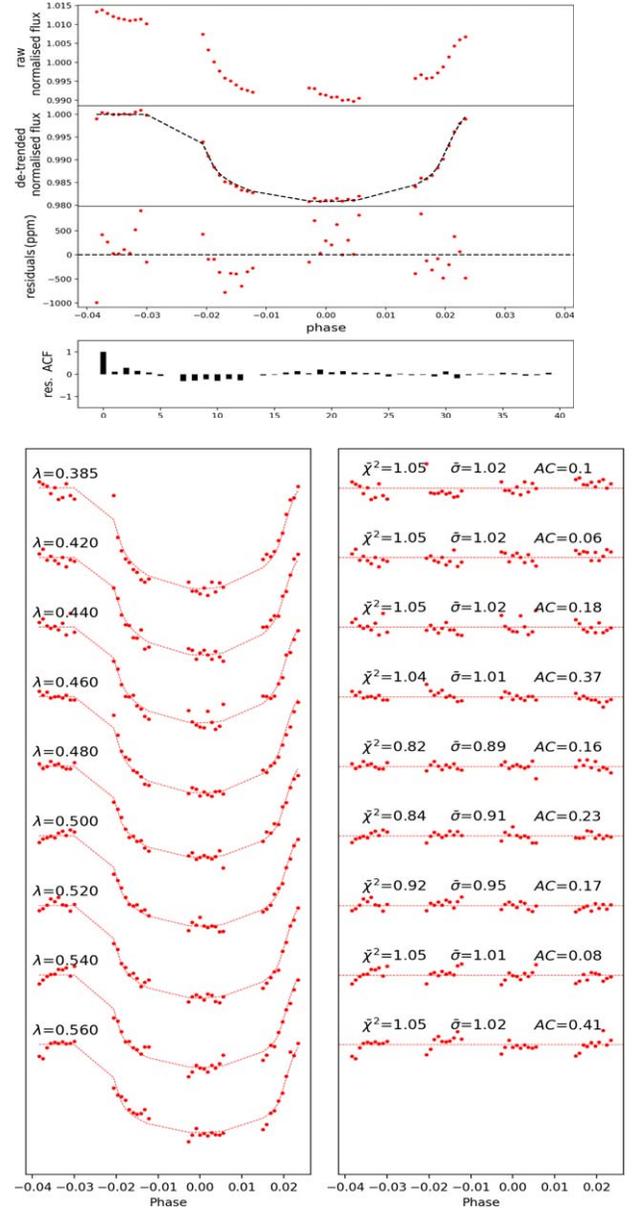
The neural network was then trained to learn the temporal variability on the pre-ingress and post-egress parts of the photometric light curve. While the stellar flux is masked during transit and then predicted autoregressively, the 2D Gaussian centroid time series is used as a covariate time series during the whole observation. This allows us to leverage its correlations with the photometric light curve and infer the systematics during the transit while excluding the planetary signal. However, intermediate transit fits are performed during training on the temporary detrended light curve in order to keep track of the model's progress and provide an additional stopping criterion. A first run is done with large margins around the expected ingress and egress times to ensure that the transits do not overlap with the training ranges. The margins are then refined after this first run to include 105% of the transit duration centered on the mid-transit time. In practice, the results are very stable and unaffected by the chosen margins provided that these remain low (under ≈ 10% of the transit duration). Several architecture and learning parameters are then tested. In both cases we find that two LSTM layers of 512 units and 10% dropout trained with an Adam optimizer and decay rate of $\beta = 0.95$ provide an optimal residual noise after the transit fit while avoiding overfitting. After the model was trained for 50 epochs, the best network—i.e., with the lowest residual noise—is saved along with the corresponding detrended light curve, obtained by dividing the raw light curve by the network's prediction. A final transit fit is performed using a Markov

---
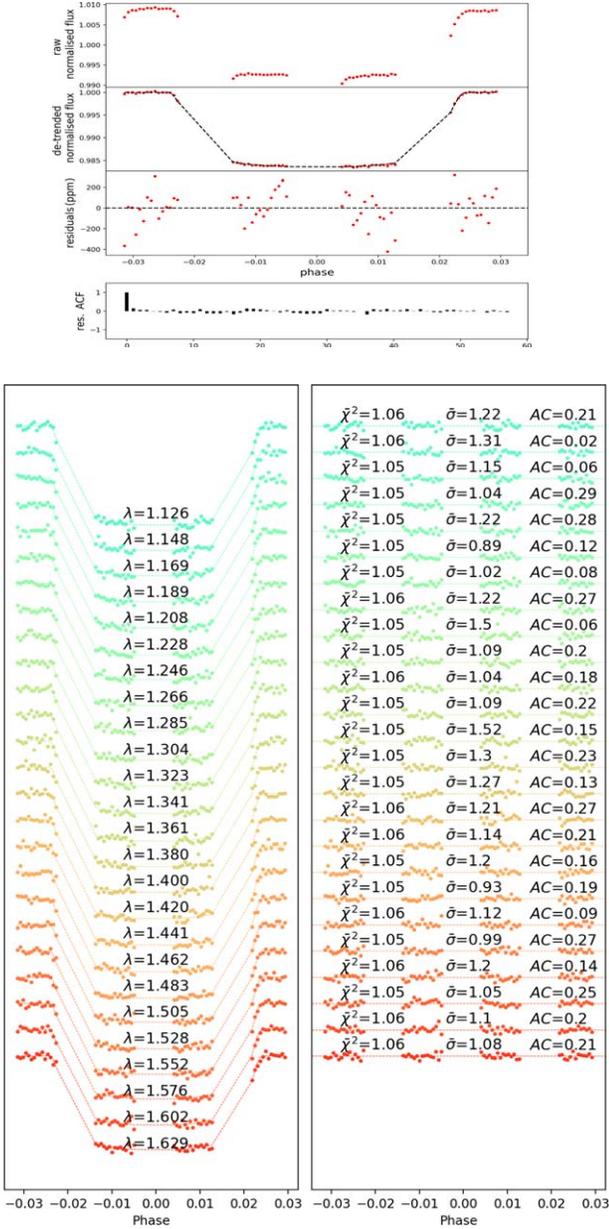
Figure 2. Top: white light curve for the HST/WFC3 G141 transmission observations of WASP-17 b. First panel: raw light curve, after normalization. Second panel: light curve, divided by the best-fit model for the systematics. Third panel: residuals for the best-fit model. Fourth panel: autocorrelation function of the residuals. Bottom: spectral light curves fitted with Iraclis for the HST/WFC3 G141 transmission spectra, where, for clarity, an offset has been applied. Left panel: the detrended spectral light curves with the best-fit model plotted. Right panel: fitting residuals with values for the χ^2, the standard deviation of the residuals with respect to the photon noise ($\bar{\sigma}$), and the autocorrelation (AC) of the residuals.

Figure 3. Top: white light curve for the HST/STIS G430L transmission observation taken on 2012 June 8 of WASP-17 b. First panel: raw light curve, after normalization. Second panel: light curve, divided by the best-fit model for the systematics. Third panel: residuals for the best-fit model. Fourth panel: autocorrelation function of the residuals. Bottom: spectral light curves fitted with Iraclis for the same observation, where, for clarity, an offset has been applied. Left panel: the detrended spectral light curves with the best-fit model plotted. Right panel: fitting residuals with values for the χ^2, the standard deviation of the residuals with respect to the photon noise ($\bar{\sigma}$), and the autocorrelation (AC) of the residuals.

Chain Monte Carlo procedure embedded in the PyLightcurve package (Tsiaras et al. 2016b). Both during and after training, the fixed planetary parameters used are those listed in Table 1 or computed using the ExoTETHyS open package (Morello et al. 2020), while the mid-transit time and R_p/R_* were left free. The raw and detrended Spitzer light curves are shown in Figure 6 (top: IRAC channel 1; bottom: IRAC channel 2), and the corresponding transmission data is available in Table 6, Appendix A. The full list of parameters used to train the network is available in Table 7, Appendix B.

2.4. Atmospheric Modeling

The spectrum resulting from our data reduction process is shown in Figure 7. Each STIS data set is indicated with a different color depending on the date on which the observation was taken. WFC3 and Spitzer data are shown in blue and purple, respectively, independently of the grism or channel employed. From the aforementioned plot we can easily notice divergent results coming from the two STIS/G430L observations, namely, those taken on 2012 June 8 and 2013 March 15. For this reason we decided to model the observed spectrum in
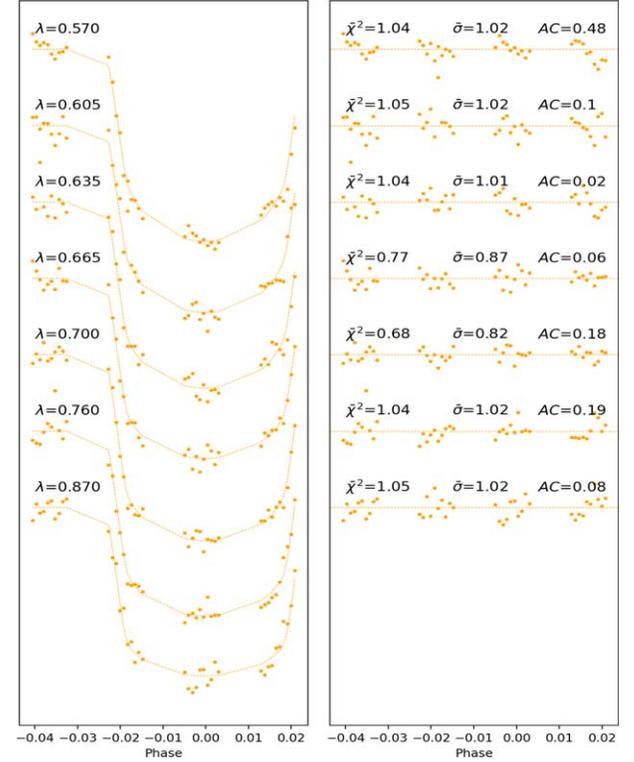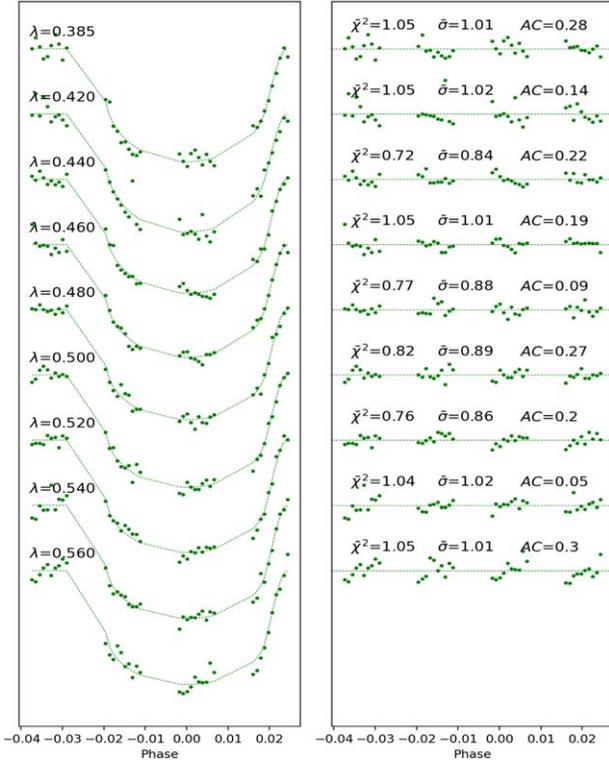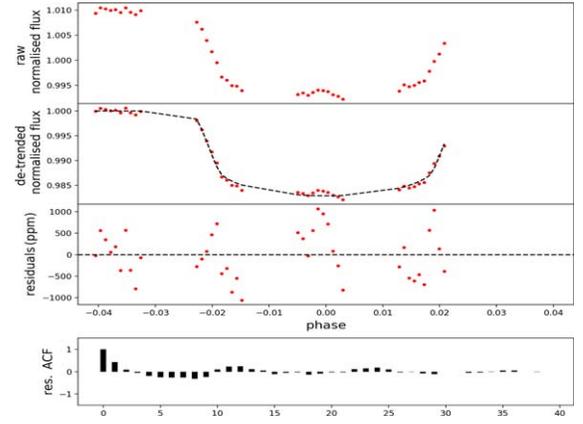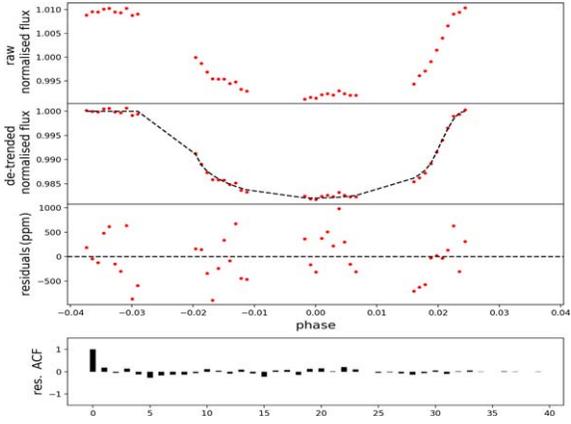
Figure 4. Top: white light curve for the HST/STIS G430L transmission observation taken on 2013 March 15 of WASP-17 b. First panel: raw light curve, after normalization. Second panel: light curve, divided by the best-fit model for the systematics. Third panel: residuals for the best-fit model. Fourth panel: autocorrelation function of the residuals. Bottom: spectral light curves fitted with Iraclis for the same observation, where, for clarity, an offset has been applied. Left panel: the detrended spectral light curves with the best-fit model plotted. Right panel: fitting residuals with values for the χ^2, the standard deviation of the residuals with respect to the photon noise ($\bar{\sigma}$), and the autocorrelation (AC) of the residuals.

Figure 5. Top: white light curve for the HST/STIS G750L transmission observation taken on 2013 March 19 of WASP-17 b. First panel: raw light curve, after normalization. Second panel: light curve, divided by the best-fit model for the systematics. Third panel: residuals for the best-fit model. Fourth panel: autocorrelation function of the residuals. Bottom: spectral light curves fitted with Iraclis for the same observation, where, for clarity, an offset has been applied. Left panel: the detrended spectral light curves with the best-fit model plotted. Right panel: fitting residuals with values for the χ^2, the standard deviation of the residuals with respect to the photon noise ($\bar{\sigma}$), and the autocorrelation (AC) of the residuals.

three separate scenarios. Case 1 includes STIS visits 2012 June 8 (visit 1) and 2013 March 19 (visit 3), WFC3 and Spitzer data, while in Case 2 we aimed to model STIS visits 2013 March 15 (visit 2) and 2013 March 19 (visit 3), WFC3 and Spitzer data sets. Additionally, we investigated the spectrum constituted by the WFC3 observations only (Case 3), thus discarding the inconsistencies of the STIS observations.

In Figure 7 we compare our data with the analysis from Sing et al. (2016). We observe that our STIS visit 1, STIS visit 3, WFC3/G141, and Spitzer data agree with the previous analysis by Sing et al. (2016), finding, however, an inconsistency with

the data point at 0.6 μm. Additionally, we notice that our STIS visit 2 data do not have a counterpart in the analysis by Sing et al. (2016), although their study claims to have analyzed all STIS observations available. We believe that their approach consisted in performing a weighted average of STIS visit 1 + 2, but we cannot be sure, as this information is not included in their methodology.

In each spectral case, we modeled the atmosphere at the terminator of WASP-17 b using the open-source atmospheric retrieval framework TauREx 3 (Al-Refaie et al. 2021). As is customary for hot Jupiters, we assumed this exoplanetary
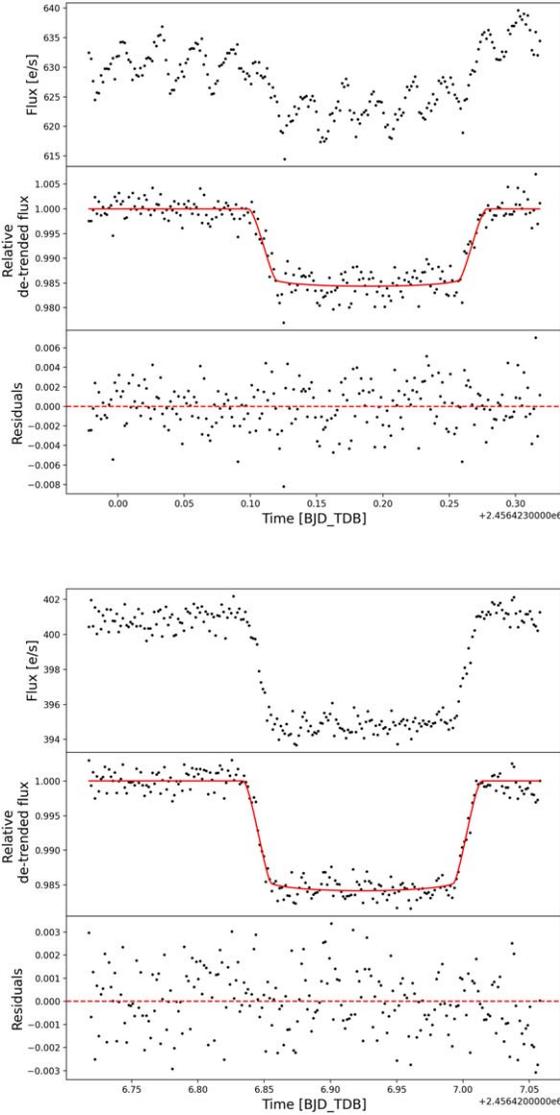
Figure 6. Raw light curves (first panel), detrended light curves (second panel), and residuals (third panel) for IRAC observations of WASP-17 b with channel 1 (top) and channel 2 (bottom).

atmosphere to be mainly constituted by H_2 and He in a ratio of 0.17. Given the short orbital period and an unconstrained eccentricity, we expect a tidally locked exoplanet with an equilibrium temperature that remains constant throughout the whole orbit around the host star. Using the equation

$$T_p = T_* \sqrt{\frac{R_*}{2a}} \left(\frac{1 - A}{\epsilon} \right)^{\frac{1}{4}}, \qquad (3)$$

we estimated the equilibrium temperature to be $T_p = 1769$ K when assuming $A = 0.1$ and $\epsilon = 0.8$. However, since we cannot ascertain the exact albedo and emissivity of the planet, we considered some extreme cases that produce a range where we expect the planetary temperature to fall. For instance, if we assume WASP-17 b to possess an albedo of 0.5 and an emissivity of 0.7 (analog to Jupiter), the planetary equilibrium temperature suddenly drops to $T_p = 1579$ K. If, instead, we consider the case of a planet that reflects a tiny amount of incoming light ($A = 0.1$) and reemits some energy (possibly energy left over from the planet's formation process) with

$\epsilon = 0.7$, then the equilibrium temperature increases to $T_p = 1829$ K.

As a result of the broad wavelength coverage of the combined observations and the high planetary equilibrium temperature (Sharp & Burrows 2007), we explored the presence of a variety of molecular opacities, ranging from the optical (TiO, McKemmish et al. 2019; VO, McKemmish et al. 2016; FeH, Dulick et al. 2003; Wende et al. 2010; SiH, Yurchenko et al. 2018; TiH, Gharib-Nezhad et al. 2021; AlO, Patrascu et al. 2015; K, Allard et al. 2019; Na, Allard et al. 2019) to the near-infrared and infrared absorbers (H_2O, Polyansky et al. 2018; CH_4, Yurchenko & Tennyson 2014; CO, Li et al. 2015; CO_2; NH_3, Coles et al. 2019), by employing the line lists from the ExoMol (Tennyson et al. 2016; Chubb et al. 2021), HITEMP (Rothman et al. 2010; Rothman & Gordon 2014), HITRAN (Rothman et al. 1987; Gordon et al. 2016), and NIST (Kramida 2013) databases.

In our final retrievals we considered only the presence of H_2O, AlO, TiH, SiH, CO, and CH_4 as trace gases. The molecular profile of each species was set to be constant at each atmospheric layer. Additionally, collision-induced absorption (CIA) from H_2-H_2 (Abel et al. 2011; Fletcher et al. 2018) and H_2-He (Abel et al. 2012), Rayleigh scattering for all molecules, and the presence of gray clouds and hazes modeled with the Lee et al. (2013) parameterization were included. We also modeled the contamination of the host star on the spectrum of WASP-17 b using the formalization by Rackham et al. (2018, 2019).

We assumed a planetary atmosphere constituted by 100 layers in a plane-parallel geometry, uniformly distributed in log space between 10^{-5} and 10^6 Pa. The temperature structure was modeled with an isothermal $T - p$ profile. The trace gases considered were allowed to vary freely between 10^{-12} and 10^{-1} in volume mixing ratio, while the planetary equilibrium temperature, T_p, could vary between 500 and 3000 K. Regarding the hazes, their top pressure P_{Mie}^{top} ranged from 10^{-4} to 10^6 Pa, the radius of the particles R_{Mie}^{Lee} ranged between 10^{-3} and 1 μm, and the Mie cloud mixing ratio χ_{Mie}^{Lee} could change between -30 and -4 in log space. Furthermore, we included a layer of gray clouds, whose top pressure could vary between 10^{-1} and 10^6 Pa (Robinson & Catling 2014; Kawashima & Ikoma 2018; Charnay et al. 2021). Lastly, the planetary radius bounds were set between 1 and 2 R_J. The prior bounds employed for each fitted parameter are reported in Table 2.

We investigated the parameter space with the nested sampling algorithm MultiNest (Feroz et al. 2009) with 750 live points and an evidence tolerance of 0.5.

2.5. Stellar Modeling

We attempted to explain the steep downward slope in the blue wavelengths of STIS visit 2 observation (see Figure 7) by modeling the effect of a combination of unocculted stellar spots and faculae on the Case 2 transmission spectrum of WASP-17 b. We accounted for solar size spots and faculae to be homogeneously distributed on the stellar surface. Current stellar models and observational evidence (Mamajek & Hillenbrand 2008; Ciardi et al. 2011; Rackham et al. 2017, 2019) show that the variability of F dwarfs is $\sim$0.1%, with a minimum of 0.07% and a maximum of 0.36%. This is one of the lowest among all stellar spectral types, with the stellar variability being inversely proportional to the
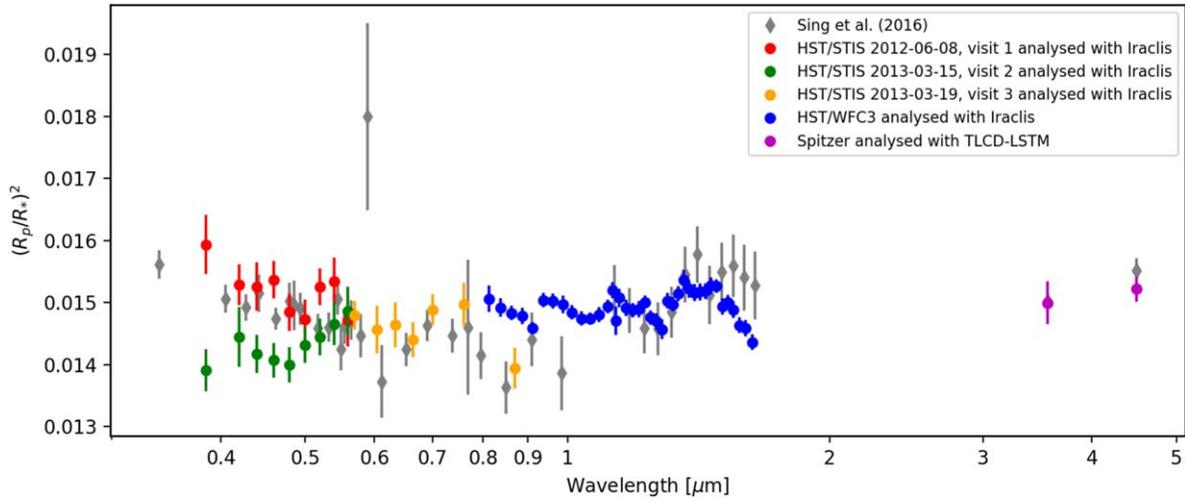
Figure 7. Transmission spectrum of WASP-17 b, constituted by HST/STIS, HST/WFC3, and Spitzer/IRAC channel 1 and 2 data analyzed in this study compared to the data from Sing et al. (2016).

Table 2
List of the Parameters, Their Prior Bounds, the Scale Used, and the Retrieved Values (Median and Standard Deviation) for the Case 1–3 Spectra Assuming an Isothermal Atmospheric Profile

Retrieved Parameters	Prior Bounds	Scale	Case 1 STIS 1&3, WFC3, IRAC	Case 2 STIS 2&3, WFC3, IRAC	Case 3 WFC3
			Retrieval Accounting for an Active Star		
R_p (R_J)	1 ; 2	linear	$1.64^{+0.03}_{-0.04}$	1.59 ± 0.04	$1.61^{+0.03}_{-0.04}$
$T_{\rm spot}$ (K)	4000 ; 5000	linear	$4367.85^{+296.58}_{-231.81}$	$4306.83^{+267.22}_{-196.70}$	$4329.70^{+278.98}_{-206.75}$
$T_{\rm fac}$ (K)	6600 ; 7000	linear	$6741.68^{+73.49}_{-58.01}$	$6919.28^{+53.01}_{-40.73}$	$6914.43^{+55.02}_{-47.08}$
$F_{\rm spot}$	0.0 ; 0.9	linear	0.13 ± 0.03	$0.19^{+0.04}_{-0.03}$	0.20 ± 0.04
$F_{\rm fac}$	0.0 ; 0.9	linear	$0.51^{+0.21}_{-0.18}$	$0.43^{+0.11}_{-0.10}$	0.50 ± 0.16
T (K)	500 ; 3000	linear	$1415.28^{+230}_{-194.43}$	$1539.70^{+317.21}_{-304.42}$	$1396.20^{+291.34}_{-243.79}$
H_2O	−12 ; −1	$\log_{10}$	$-3.20^{+0.99}_{-0.60}$	$-1.93^{+0.39}_{-0.70}$	$-2.19^{+0.55}_{-0.69}$
AlO	−12 ; −1	$\log_{10}$	$-7.94^{+0.87}_{-0.81}$	$-9.68^{+1.55}_{-1.42}$	$-6.39^{+0.81}_{-1.41}$
TiH	−12 ; −1	$\log_{10}$	$-9.70^{+1.01}_{-1.14}$	$-7.91^{+0.98}_{-1.70}$	$-7.82^{+1.10}_{-1.59}$
SiH	−12 ; −1	$\log_{10}$	$-8.39^{+2.25}_{-2.21}$	$-7.03^{+2.24}_{-2.84}$	$-7.08^{+3.02}_{-3.05}$
CH_4	−12 ; −1	$\log_{10}$	-8.34 ± 2.24	$-7.48^{+2.55}_{-2.72}$	$-8.08^{+2.34}_{-2.24}$
CO	−12 ; −1	$\log_{10}$	$-7.09^{+2.97}_{-3.01}$	$-6.51^{+3.15}_{-3.36}$	$-7.55^{+3.03}_{-2.77}$
$P_{\rm clouds}$ (Pa)	−1 ; 6	$\log_{10}$	$4.11^{+1.19}_{-1.48}$	$1.95^{+0.48}_{-0.93}$	$3.98^{+1.33}_{-1.03}$
$R_{\rm Mie}^{\rm Lee}$ (μm)	−3 ; 1	$\log_{10}$	$-1.24^{+1.29}_{-1.15}$	$-1.25^{+1.29}_{-1.10}$	$-1.38^{+1.33}_{-1.03}$
$P_{\rm Mie}^{\rm top}$ (Pa)	−4 ; 6	$\log_{10}$	$2.20^{+2.56}_{-3.77}$	$2.11^{+2.44}_{-3.71}$	$2.08^{+2.36}_{-3.42}$
$\chi_{\rm Mie}^{\rm Lee}$	−30 ; −4	$\log_{10}$	$-20.90^{+8.77}_{-5.78}$	$-20.13^{+8.06}_{-6.07}$	$-19.87^{+7.91}_{-6.27}$
			Retrieval Accounting for a Homogeneous Star		
R_p (R_J)	1 ; 2	linear	1.72 ± 0.01	1.71 ± 0.01	$1.71^{+0.01}_{-0.02}$
T (K)	500 ; 3000	linear	$951.13^{+155.25}_{-120.53}$	$950.73^{+93.36}_{-83.04}$	$900.56^{+153.18}_{-112.25}$
H_2O	−12 ; −1	$\log_{10}$	$-3.22^{+0.47}_{-0.49}$	$-1.40^{+0.19}_{-0.28}$	$-2.41^{+0.48}_{-0.56}$
AlO	−12 ; −1	$\log_{10}$	$-8.06^{+0.61}_{-0.83}$	$-10.03^{+1.86}_{-1.35}$	$-7.25^{+0.87}_{-1.12}$
TiH	−12 ; −1	$\log_{10}$	$-8.48^{+0.66}_{-0.83}$	$-6.83^{+0.79}_{-1.11}$	$-7.85^{+0.82}_{-1.22}$
SiH	−12 ; −1	$\log_{10}$	$-3.85^{+1.18}_{-2.38}$	$-9.10^{+2.23}_{-1.87}$	$-7.26^{+3.20}_{-3.04}$
CH_4	−12 ; −1	$\log_{10}$	$-9.03^{+1.83}_{-1.88}$	$-8.40^{+2.24}_{-2.26}$	-8.87 ± 2.04
CO	−12 ; −1	$\log_{10}$	$-7.48^{+2.93}_{-2.91}$	$-7.03^{+3.08}_{-3.21}$	$-7.64^{+3.00}_{-2.87}$
$P_{\rm clouds}$ (Pa)	−1 ; 6	$\log_{10}$	$4.94^{+0.69}_{-0.71}$	$4.31^{+1.06}_{-1.00}$	$4.74^{+0.80}_{-0.91}$
$R_{\rm Mie}^{\rm Lee}$ (μm)	−3 ; 1	$\log_{10}$	$-1.53^{+1.39}_{-1.01}$	$-1.12^{+1.31}_{-1.24}$	$-1.47^{+1.43}_{-1.01}$
$P_{\rm Mie}^{\rm top}$ (Pa)	−4 ; 6	$\log_{10}$	$1.89^{+2.95}_{-3.90}$	$2.67^{+2.22}_{-4.42}$	$1.87^{+2.88}_{-3.75}$
$\chi_{\rm Mie}^{\rm Lee}$	−30 ; −4	$\log_{10}$	$-20.75^{+8.37}_{-6.07}$	$-20.63^{+9.05}_{-6.04}$	$-20.88^{+8.56}_{-6.01}$

temperature of the star (McQuillan et al. 2014). Though generally FGK stars are mostly inactive and do not contaminate the transmission spectrum of the planets orbiting them, their active counterparts do, and great care must be taken when analyzing the planetary spectra that they pollute.

According to Rackham et al. (2019), for FGK-type stars the stellar spot temperature can be calculated as

$$T_{\text{spot}} \, [\text{K}] = 0.418 \, T_{\text{phot}} + 1620 \quad (4)$$

and the faculae temperature as

$$T_{\text{fac}} \, [\text{K}] = T_{\text{phot}} + 100, \quad (5)$$

with T_{phot} being the temperature of the stellar photosphere, in our study equal to 6550 ± 80 K. The spectral emission density of the heterogeneous star is modeled using the BT-Settl models (Allard et al. 2013), and the stellar spectral model grid is generated using the PHOENIX library (Husser et al. 2013). In essence, the spots and faculae are modeled as separate cooler and hotter stars, respectively (A. Thompson et al. 2022, in preparation). The stellar emission densities (SEDs) of the three surface components (spots, faculae, and quiescent photosphere) are then combined in the ratio of their covering fractions to produce the observed disk-integrated stellar spectrum

$$S_{\text{star},\lambda} = ((1 - F_{\text{spot}} - F_{\text{fac}}) \times S_{\text{phot},\lambda}) \\ + (F_{\text{spot}} \times S_{\text{spot},\lambda}) + (F_{\text{fac}} \times S_{\text{fac},\lambda}), \quad (6)$$

where $S_{\text{star},\lambda}$ is the flux of the heterogeneous star at a given wavelength; $S_{\text{phot},\lambda}$, $S_{\text{spot},\lambda}$, and $S_{\text{fac},\lambda}$ are the spectra of the quiet photosphere, the starspots, and the faculae at the same wavelength, respectively; and F_{spot} and F_{fac} are the covering fractions of the spots and faculae with respect to the observed stellar disk.

Compared to the nominal transit depth, the effect of a heterogeneous star produces a wavelength-dependent offset on the transmission spectrum given by

$$\epsilon_{\lambda, s+f} = \frac{1}{1 - F_{\text{spot}} \left(1 - \frac{S_{\lambda, spot}}{S_{\lambda, \text{phot}}} \right) - F_{\text{fac}} \left(1 - \frac{S_{\lambda, \text{fac}}}{S_{\lambda, \text{phot}}} \right)}, \quad (7)$$

where F_{spot} and F_{fac} are the covering fractions of the spots and faculae and $S_{\lambda, \text{spot}}$, $S_{\lambda, \text{fac}}$, and $S_{\lambda, \text{phot}}$ are the emitted fluxes of the spots, faculae, and immaculate photosphere at a given wavelength, respectively. An important limitation to consider is that this simplistic method of modeling stellar active regions may be inaccurate, particularly with respect to faculae modeling, as it fails to describe any center-to-limb variations that they may exhibit or their strong dependence on magnetic field strength (Norris et al. 2017). However, given the precision of the observations in question, this simplified stellar model should be sufficient to begin to investigate any potential heterogeneity displayed by WASP-17.

In our retrievals, we considered a varying spot temperature between 4000 and 5000 K and a faculae temperature between 6600 and 7000 K. Both the spots and faculae coverage fraction bounds were set between 0.0 and 0.9 of the total stellar surface.

We tested the possibility of a variable stellar photosphere also on the spectrum in Cases 1 and 3.

3. Results

3.1. Retrievals Accounting for an Active Star

When comparing the posteriors for each of the three cases in Figure 8, one can find common atmospheric features that are stable independently of the data sets modeled. First, the planetary temperatures retrieved are within 1σ of each other, and their upper bounds are inside the limits of the equilibrium temperature [1579 K; 1829 K] calculated in Section 2.4. Similarly, the planetary radii at 10 bars are compatible with one another.

All three spectra agree on a number of aspects: the presence of water in the solar/supersolar regime, which is consistent with the result from Pinhas et al. (2018), $\log_{10}(\text{H}_2\text{O}) = -4.04^{+0.91}_{-0.42}$. The reference solar water abundance was calculated under thermochemical equilibrium at a pressure of 1 bar for the equilibrium temperature of WASP-17 b, and it is equal to $\log_{10}(X^{\odot}_{\text{H}_2\text{O}}) = -3.3$ (Pinhas et al. 2018).

Our results suggest the presence of AlO and TiH on the order of 10^{-8} in volume mixing ratio, unconstrained SiH, and haze nondetection. Furthermore, the retrievals indicate a strong stellar contamination on the spectrum of WASP-17 b in the WFC3 data set too, where we do not expect stellar activity to play a big part. In all three scenarios we retrieved a spot temperature of around 4300 K, as well as spot and faculae covering fractions of the star on the order of 10%–20% and 40%–50%, respectively. Our results report a faculae temperature in the Case 1 transmission spectrum between 33 and 165 K higher than what Equation (5) predicts. On the other hand, T_{fac} on Case 2 and Case 3 spectra is between 217 and 322 K higher than expected ($T_{\text{fac}} = 6919.28^{+53.01}_{-40.73}$ and $T_{\text{fac}} = 6914.43^{+55.02}_{-47.08}$). Although the study by Rackham et al. (2018) does not provide typical uncertainties on the temperature of spots and faculae, we can easily compare the retrieved values with the stellar photospheric uncertainty (~80 K) from Table 1. Hence, the T_{fac} retrieved in Case 1, being less than 2σ away from the 80 K uncertainty, could be deemed acceptable compared to the faculae temperature in Cases 2 and 3, which is three to four times above the 80 K limit.

In Case 2 and Case 3 spectra we find supersolar water abundances ($\log_{10}(\text{H}_2\text{O}) = -1.93^{+0.39}_{-0.70}$ and $\log_{10}(\text{H}_2\text{O}) = -2.19^{+0.55}_{-0.69}$, respectively), while Case 1 returns a $\log_{10}(\text{H}_2\text{O}) = -3.20^{+0.99}_{-0.60}$, being $0.97 \times$ solar and 0.79 times the result reported by Barstow et al. (2016), equal to 5×10^{-4}. Depending on the spectral scenario considered, the AlO, TiH, and SiH abundances retrieved differ (Case 1: $\log_{10}(\text{AlO}) = -7.94^{+0.87}_{-0.81}$, $\log_{10}(\text{TiH}) = -9.70^{+1.01}_{-1.14}$, $\log_{10}(\text{SiH}) = -8.39^{+2.25}_{-2.21}$; Case 2: $\log_{10}(\text{AlO}) = -9.68^{+1.55}_{-1.42}$, $\log_{10}(\text{TiH}) = -7.91^{+0.98}_{-1.70}$, $\log_{10}(\text{SiH}) = -7.03^{+2.24}_{-2.84}$; Case 3: $\log_{10}(\text{AlO}) = -6.39^{+0.81}_{-1.41}$, $\log_{10}(\text{TiH}) = -7.82^{+1.10}_{-1.59}$, $\log_{10}(\text{SiH}) = -7.08^{+3.02}_{-3.05}$), yet they are compatible with one another being within their 1σ confidence band. According to the thermochemical equilibrium model GGChem (Woitke et al. 2018), the expected abundance of AlO and TiH at $p = 1$ bar and $T = \sim1400$ K is $\sim10^{-11}$ and $\sim10^{-12}$ in volume mixing ratio, respectively. The theoretical estimate is in accordance with the retrieved AlO abundance in Case 2, where we find a lower bound equal to $\log_{10}(\text{AlO}) = -11.1$. However, in all other cases for both AlO and TiH, the retrieved abundances are $3\sigma - 4\sigma$ away from the expected values. On the contrary, the retrieved uncertainties on the SiH abundances are in agreement with the theoretical
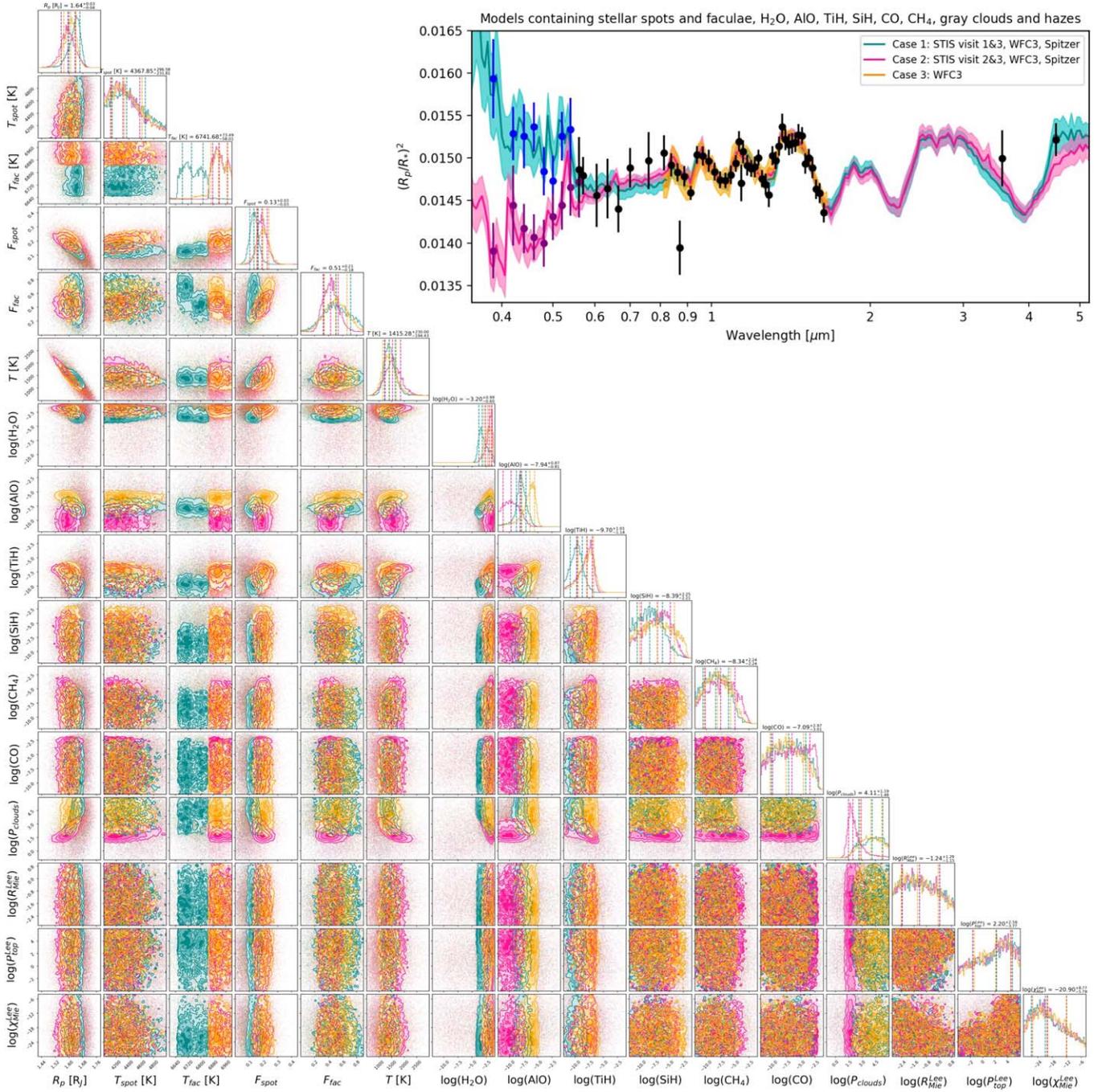
Figure 8. Posterior distributions for the transmission spectrum of WASP-17 b accounting for an active star retrieved with different data sets. The dashed vertical lines in each histogram refer to the median value, the first quantile (lower bound error), and the third quantile (upper bound error) of each parameter. Similarly, the reported values on top of the histograms denote the parameter's median value, the first quantile, and the third quantile. The values shown are those obtained with the spectrum constituted by STIS visit 1&3, WFC3, Spitzer (Case 1). Inset: transmission spectra with best-fit models and their 1σ uncertainties.

value computed at $p = 1$ bar and $T = \sim1400$ K, it being $\log_{10}(\mathrm{SiH}) = \sim-10$.

We retrieve conflicting results for the cloud deck. The Case 1 and Case 3 posteriors returned a mean cloud deck at a pressure of $\sim1.1 \times 10^4$ Pa corresponding to ~0.11 bars. In Case 2 the cloud top pressure is higher in the atmosphere, at a pressure of 0.9 mbar. The cloud coverage found at higher altitudes could be caused by the retrieval framework trying to fit the downward slope created by the STIS visit 2 data in the optical range,

which cannot be explained by any molecular absorber. The clouds cut off any molecular signature in the optical, leaving just the tip of two particular TiH and SiH signatures visible at 0.54 and 0.42 μm in the Case 2 spectrum.

Figure 10 in Appendix C shows Case 1 data fitted by the best-fit model accounting for stellar activity and the contributions of active trace gases, CIA, clouds, and hazes to the fit.

We report the retrieval results for each spectral case in Table 2 (upper part).
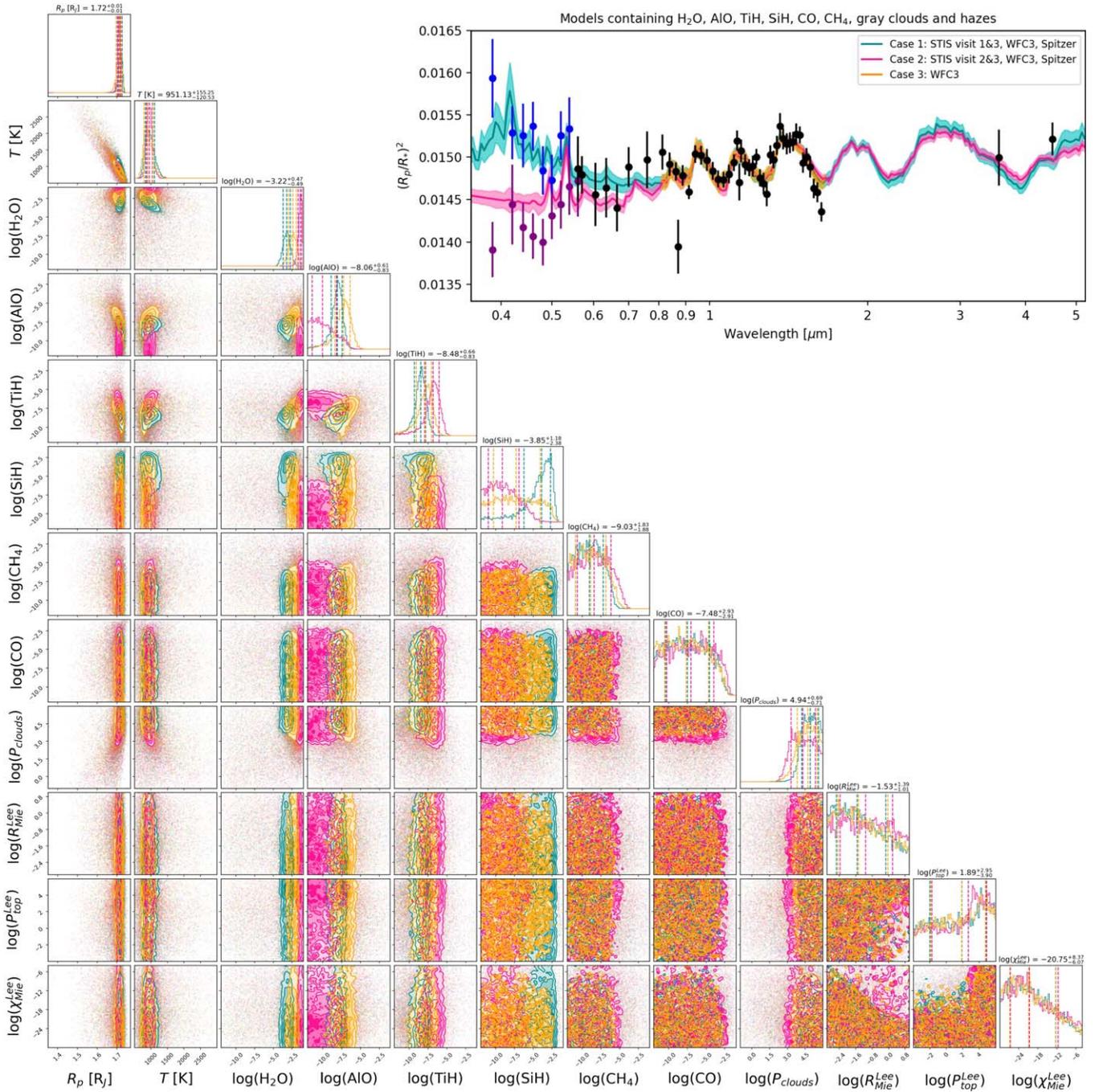
Figure 9. Posterior distributions for the transmission spectrum of WASP-17 b accounting for a homogeneous star retrieved with different data sets. The dashed vertical lines in each histogram refer to the median value, the first quantile (lower bound error), and the third quantile (upper bound error) of each parameter. Similarly, the reported values on top of the histograms denote the parameter's median value, the first quantile, and the third quantile. The values shown are those obtained with the spectrum constituted by STIS visit 1&3, WFC3, Spitzer (Case 1). Inset: transmission spectra with best-fit models and their 1σ uncertainties.

3.2. Retrievals Accounting for a Homogeneous Star

We modeled the three spectral scenarios previously identified by accounting for the same molecular and atmospheric parameters. However, in this instance we modeled the star as a homogeneous body. We find that the absence of stellar activity does not impact the molecular detections, but it does affect a few of the retrieved abundances (Figure 9).

As in the previous case, our data suggest the presence of water, aluminum oxide, and titanium hydride. Our retrievals return solar $\log_{10}(H_2O) = -3.22^{+0.47}_{-0.49}$ and supersolar

$\log_{10}(H_2O) = -2.41^{+0.48}_{-0.56}$ and $\log_{10}(H_2O) = -1.40^{+0.19}_{-0.28}$ water concentrations when modeling the Case 1, Case 3, and Case 2 spectrum, respectively. The last two results indicate a higher abundance than what current theories predict for hot Jupiters ($\log_{10}(H_2O) = \sim-3.3$; Venot et al. 2012; Venot & Agúndez 2015; Woitke et al. 2018).

The AlO and TiH abundances retrieved from the Case 3 spectrum appear to be more compatible with those retrieved from Case 1. However, both the AlO and the TiH results obtained from each of the three cases are within their respective 1σ uncertainties. These results are not consistent with chemical

equilibrium models, as Woitke et al. (2018) predict a volume mixing ratio of roughly 10^{-16} for AlO and 10^{-18} for TiH at a pressure of 1 bar and $T = \sim 900$ K. The discrepancies could be caused by chemical disequilibrium processes, e.g., photochemistry (Venot et al. 2015; Fleury et al. 2019) or quenching (Shulyak et al. 2020), occurring in the atmosphere of WASP-17 b.

SiH is still largely undetected in Case 2 and Case 3 spectra. On the other hand, exceptionally high amounts of this trace gas are detected in Case 1. We recognize that such a large contribution ($\log_{10}(\mathrm{SiH}) = -3.85^{+1.18}_{-2.38}$) is unlikely, as theoretical models (Woitke et al. 2018) predict a SiH volume mixing ratio of $\sim 10^{-16}$ at 1 bar and at ~ 900 K. Moreover, all three spectra return a consistent median planetary radius, temperature, and cloud coverage, approximately equal to 1.71 R_J, 930 K, and 4.6×10^4 Pa, respectively.

In place of stellar faculae, a Mie scattering haze could have explained the upward slope in the Case 1 spectrum. Unfortunately, this option is refused by the retrieval, which is not able to constrain any of the aerosol parameters: particle size $R_{\mathrm{Mie}}^{\mathrm{Lee}}$, top pressure $P_{\mathrm{Mie}}^{\mathrm{top}}$, and mixing ratio $\chi_{\mathrm{Mie}}^{\mathrm{Lee}}$. Even when we test the aerosols' presence in the simplest model containing only water and clouds, their posterior distributions are completely unconstrained.

The retrieved values for each atmospheric parameter are reported in Table 2 (bottom part), while Figure 11 in Appendix C shows Case 2 data fitted by the best-fit model and the contributions of active trace gases, CIA, clouds, and hazes to the fit.

4. Discussion

WASP-17 b has been observed, studied, and modeled intensively in the past (e.g., Anderson et al. 2011; Mandell et al. 2013; Pinhas et al. 2018; Goyal et al. 2020) by employing observations taken with WFC3/G141 (staring mode), HST/STIS, and Spitzer. Our study, complementary to the work by Alderson et al. (2022), offers a consistent analysis performed by combining and reducing in a reproducible manner all currently available WASP-17 b transmission data obtained with space-based observatories. We include all public STIS and IRAC data, plus WFC3/G141 and WFC3/G102 observations, both taken in spatial scanning mode. This large breadth of observations allows us to investigate the planet's atmospheric spectrum spanning the wavelengths from the optical to the near-infrared.

The combination of several data sets has its pros and cons. By coupling observations taken at different wavelengths, we are able to achieve a broad wavelength coverage, paramount to obtaining more precise measurements and unambiguous molecular detection. It is extremely challenging to absolutely calibrate data obtained from different detectors, especially if each of them targets a very specific spectral range with a limited or even absent wavelength overlap (Yip et al. 2020). Moreover, each instrument creates its own distinct systematics that need to be modeled ad hoc.

The STIS detector shares a short portion of the wavelength space, about 0.14 μm, with WFC3. This wavelength overlap is useful to investigate potential calibration discrepancies between instruments. In the 0.8–0.94 μm range, our spectrum displays six WFC3/G102 data points and one STIS/G750L point (Figure 7). The response of the STIS G750L grating shows a strong dip above 0.8 μm (Prichard et al. 2022); hence, the last

spectral bin (0.8–0.94 μm) has a flux rate $\sim$50% lower than the rest of the bands, and it is possibly subject to different systematics. Because of the shape of the transmission curve, we opted to increase the size of the final spectral bin to counteract the flux loss. Our analysis returns an STIS data point at 0.87 μm that is at least 2σ away from the G102 data points placed between 0.8 and 0.94 μm. A similar decrease in transit depth at the same wavelengths was also recovered by Sing et al. (2016), as can be seen in Figure 7. Yet the transit depths of the white light curves for G750L and G102 are within 1σ of each other (WFC3/G102: $R_p/R_* = 0.12184^{+0.00019}_{-0.00022}$; STIS/G750L: $R_p/R_* = 0.1211^{+0.0014}_{-0.0013}$), confirming that the two instrumental calibrations are in overall agreement. Finally, we must note that this problematic STIS/G750L data point is not statistically significant for the spectral modeling. From Figures 8 and 9 we can observe that the TauREx 3 atmospheric model ignores this data point when computing the best-fit spectrum.

On the other hand, between 3 and 5 μm lie the Spitzer data points, whose transit depths cannot be compared to any additional data set. We shifted the two Spitzer data points 100 ppm up and 100 ppm down from their original position to see whether the results would be considerably impacted. In either case the retrieved mean molecular abundances and other atmospheric features, such as radius and temperature, fluctuate at the order of the fifth decimal figure from the initial values, implying an accurate data reduction process and stability of the results.

An additional issue to take into account when combining data sets taken months or even years apart is atmospheric variability. We must remember that planets are dynamic bodies, varying in space and time. Hence, mechanisms like star–planet interaction and global circulation processes such as polar vortexes and zonal jets can produce very strong temperature and chemical differences (Cho et al. 2003, 2021). It might not be surprising that the same planet can display contrasting spectral features at the same wavelengths, such as the two opposite spectral trends we presented between $\sim$0.4 and $\sim$0.6 μm. In light of this, we must stress that the publicly available STIS observations used in this study lack the post-egress part of the planetary transit (Figures 3, 4, 5). Missing light-curve data strongly impact the transit fit model, which then could potentially affect the derived transit depth, leading to discordant spectral features among different observations, as highlighted in Figure 7.

Due to the discrepancies in the data, we decided to model the contrasting STIS data sets separately: in Case 1 we considered a spectrum that includes STIS visit 1&3, WFC3, and IRAC; in Case 2 we modeled the spectrum with STIS visit 2&3, WFC3, and IRAC. Additionally, we employed the WFC3 observations alone (Case 3) to check how the results would change when we do not include the problematic STIS data sets.

To explain the unusually strong downward slope in the optical range displayed by the Case 2 spectrum (Figure 8, inset), an active star was included in the retrieval setup. For consistency, we applied the same stellar model to Case 1 and Case 3 spectra. Potentially, STIS visits 2&3, being taken just a few days apart, were impacted by a stellar event, causing the spectrum to be best fitted by a model containing high spot and faculae covering fractions. STIS visit 1 could have also been affected by a similar event, given that its best model favors stellar activity in place of aerosols.

Theoretically, a faculae covering fraction between 40% and 50% is unlikely in an F6-type star like WASP-17, unless we are dealing with a rare and extreme event. Moreover, we recognize that the posterior distributions between the faculae temperature and their covering fraction are degenerate (see Figure 8). This is because the retrieval is unable to distinguish between two scenarios: (1) a smaller covering fraction of hotter faculae and (2) a larger covering fraction of cooler faculae. Both scenarios result in similar stellar disk-integrated SEDs and thus introduce similar contamination features to the transmission spectrum.

There are no previous studies on the activity of the star, so we are unable to compare our results with published research. However, Khalafinejad et al. (2018) mention that their attempt to identify a sodium feature in the spectrum of WASP-17 b could have been impacted by an in-transit activity of the host star, which decreased the planetary Na signal. Hence, stellar contamination cannot be excluded as an additional cause for a decreasing transit depth in the optical regime. Continuous photometric monitoring of WASP-17 is necessary to determine accurately the activity levels of the star.

When the star is treated as a homogeneous body, the retrieval of the Case 1 spectrum results in a extremely high SiH volume mixing ratio $\log_{10}(\mathrm{SiH}) = -3.85^{+1.18}_{-2.38}$. This result is unlikely, given that chemical equilibrium models predict a SiH abundance on the order of 10^{-16} at 900 K (Woitke et al. 2018). Perhaps such high SiH abundance is due to a missing molecule that is not accounted for. Either this missing gas absorbs at the same wavelengths of SiH, or it has similar absorption features. Even if we wanted to investigate this further, we do not possess all the possible molecular cross sections, and it is not feasible to test all the known molecules that absorb in the optical region. However, by inspecting the SiH results retrieved from the Case 2 and Case 3 spectra, we confirm that SiH is largely unconstrained and remains undetected.

Overall, we notice that when we consider an inactive star, the retrievals struggle to fit the data points at the end of the WFC3 wavelength coverage at ~ 1.6–$1.8\,\mu m$ and those at 0.4–0.55 μm, especially visit 2 (see Figure 9, inset). This statement is supported by the log evidence of the models: when stellar activity is included, the log(E) increases by a minimum of 4σ (compared to the same model without stellar activity). Furthermore, independently of the data sets modeled, our results suggest the presence of the same trace gases (H_2O, AlO, TiH) as when accounting for a heterogeneous star. At this stage we do not possess enough evidence to discard a particular STIS data set in favor of another one, but the information content derived by WFC3 data alone is enough to propose the existence of those species in the atmosphere of WASP-17 b.

No previous study has detected any metal hydrates or oxides in the atmosphere of this particular hot Jupiter, except Bento et al. (2014) searching for TiO signatures in the upper atmosphere of WASP-17 b. Theoretical studies by Fortney et al. (2008) propose the presence of TiO and VO in the atmosphere of planets with large day–night temperature contrasts. We do not exclude the presence of these trace gases, but our analyses favor a model containing AlO, TiH, SiH, CH_4, and CO rather than TiO, VO, and FeH by a 2.6σ evidence, when applied to the spectrum in Case 1 (Table 3). As of yet, this is the first time that the presence of AlO and TiH has been suggested in the atmosphere of WASP-17 b.

During our preliminary retrievals, we tested different models containing a variety of trace gases on the spectrum in Case 1, but ultimately we found that including H_2O, AlO, TiH, SiH, clouds, hazes, and an active star would lead to the best results. Adding CH_4 and CO in the latter model did not substantially affect the Bayesian evidence, the two models being 0.26σ away from each other.

On the other hand, the spectrum containing STIS visit 2 proved trickier to model. Out of the five models tested on these data, models (1), (3), (4) and (5) in Table 3 (middle section) were within less than 1σ of each other, and model (2) containing H_2O, AlO, TiH, SiH, CH_4, CO, clouds, and hazes was 5.64σ away from model (1), which includes the same chemical species plus stellar variability. Ultimately, we used the best-fit model for the Case 1 spectral scenario also in the Case 2 data set and on the WFC3 data alone, to make a valid comparison between the scenarios in terms of molecular abundances. The retrievals conducted exclusively on the WFC3 data also favor a model containing H_2O, AlO, TiH, SiH, clouds, hazes, stellar spots, and faculae.

Our results suggest that WASP-17 b possesses mostly a clear atmosphere, free from a thick layer of clouds and aerosols. Sing et al. (2016) report the atmosphere of this hot Jupiter to be the clearest among the 10 exoplanets in their study, presenting distinct water features. Pinhas et al. (2018) find similar results, their spectrum being fitted best by a model containing mostly a cloudless atmosphere with a cloud/haze fraction of 0.2 and a cloud top pressure of 0.1 mbar. On the other hand, Barstow et al. (2016) report the presence of scattering aerosols at relatively high altitudes, but not so strong as to reduce the size of the other molecular features. Mandell et al. (2013) also claim that their data are best fitted by a model that accounts for hazes or clouds.

We were unable to identify the alkali lines (Na, K) reported by Sing et al. (2016). Their data point at $\sim 0.6\,\mu m$ has an uncertainty three times larger than the other ones, and it is not statistically significant to demonstrate the presence of sodium in the atmosphere of WASP-17 b.

Furthermore, during our exploratory retrievals we did not find evidence of CO_2, which, on the contrary, is detected by Alderson et al. (2022). Due to the sparse nature of the Spitzer data points and the influence that additional molecules can impart in the spectrum of an exoplanet at the wavelengths probed by IRAC, it is challenging to place precise constraints on the abundance of carbon-bearing molecules.

Regardless of whether we consider an active star or not, the retrieved planetary temperature is always lower than the calculated equilibrium temperature, as transmission studies often find. Discrepancies between the retrieved and the calculated temperatures have been analyzed by several authors (e.g., Caldas et al. 2019; MacDonald et al. 2020; Pluriel et al. 2020b; Changeat et al. 2021) and found to arise from a combination of aspects: the adoption of 1D atmospheric models to describe the different molecular content of the morning and evening terminators, the use of simplified models to characterize the planets' 3D processes, and the adoption of incorrect assumptions regarding the albedo and the emissivity when calculating the planet's equilibrium temperature. Hence, retrieving a lower temperature than calculated should not be surprising.

Table 3
Bayesian Log-difference between Different Models Depending on the Observations Fed to the Retrievals

Setup	Log Evidence	Sigma (Discarded by)	Retrieved Temperature (K)
Case 1: STIS Visits 1 and 3, WFC3, Spitzer			
(1) H_2O, AlO, TiH, SiH, CH_4, CO, clouds, hazes, stellar activity	395.73		$1415.28^{+230.00}_{-194.43}$
(2) H_2O, AlO, TiH, SiH, CH_4, CO, clouds, hazes	389.31	4.01 w.r.t. (1)	$951.13^{+155.25}_{-120.53}$
(3) H_2O, clouds, stellar activity	395.02	1.84 w.r.t. (1)	$1429.50^{+363.20}_{-245.74}$
(4) H_2O, AlO, TiH, SiH, clouds, hazes, stellar activity	395.90	<1 w.r.t. (1)	$1397.57^{+229.83}_{-193.95}$
(5) H_2O, TiO, VO, FeH, clouds, stellar activity	393.60	2.6 w.r.t. (1)	$1854.96^{+382.33}_{-495.03}$
Case 2: STIS Visits 2 and 3, WFC3, Spitzer			
(1) H_2O, AlO, TiH, SiH, CH_4, CO, clouds, hazes, stellar activity	401.41		$1539.70^{+317.21}_{-304.42}$
(2) H_2O, AlO, TiH, SiH, CH_4, CO, clouds, hazes	387.38	5.64 w.r.t. (1)	$950.73^{+93.36}_{-83.04}$
(3) H_2O, clouds, stellar activity	401.68	<1 w.r.t. (1)	$1357.63^{+234.71}_{-263.14}$
(4) H_2O, AlO, TiH, SiH, clouds, hazes, stellar activity	401.14	<1 w.r.t. (1)	$1435.55^{+266.26}_{-282.96}$
(5) H_2O, TiO, VO, FeH, clouds, stellar activity	401.42	<1 w.r.t. (1)	$1550.71^{+306.26}_{-346.10}$
Case 3: WFC3			
(1) H_2O, AlO, TiH, SiH, CH_4, CO, clouds, hazes, stellar activity	285.37		$1396.20^{+291.34}_{-243.79}$
(2) H_2O, AlO, TiH, SiH, CH_4, CO, clouds, hazes	278.77	4.05 w.r.t. (1)	$900.56^{+153.18}_{-112.25}$
(3) H_2O, clouds, stellar activity	284.59	1.88 w.r.t. (1)	$1374.81^{+378.09}_{-262.77}$
(4) H_2O, AlO, TiH, SiH, clouds, hazes, stellar activity	285.44	<1 w.r.t. (1)	$1356.01^{+256.60}_{-220.37}$
(5) H_2O, TiO, VO, FeH, clouds, stellar activity	284.15	2.15 w.r.t. (1)	$1475.32^{+309.41}_{-311.57}$

5. Conclusion

Remote-sensing studies are the only technique through which we can unveil the atmospheric characteristics of planets outside our solar system. In recent years HST has pioneered the spectroscopic investigation of exoplanets. In this study we presented the transmission spectrum of WASP-17 b observed with the STIS and the WFC3 mounted on HST and the Infrared Camera Array aboard the Spitzer Space Telescope. The Hubble spectroscopic data were reduced with Iraclis, a specialized STIS and WFC3 data reduction routine. Photometric data obtained by Spitzer were instead reduced and analyzed with the TLCD-LSTM method by means of a long short-term memory network. Given the discordant results obtained for two STIS observations that cover the same wavelength range, we decided to model the spectrum of WASP-17 b in three separate cases: (a) including STIS visit 1&3, WFC3, IRAC (Case 1); (b) including STIS visit 2&3, WFC3, IRAC (Case 2); (c) WFC3 only (Case 3). The fully Bayesian retrieval framework TauREx 3 was then employed to find the model that can best explain each spectral scenario. Retrieval results find that the best-fit model is constituted by H_2O, AlO, TiH, SiH, clouds, hazes, and stellar activity in Cases 1 and 3. The best-fit model for Case 2 includes CH_4 and CO too; however, their addition only improved the Bayesian evidence by 0.26σ. We acknowledge that the extreme stellar activity identified on the F6-type host star is unlikely; therefore, we check whether a model containing the same trace gases but including a homogeneous star is able to describe all three spectra. Independently of the activity of the star, our analysis indicates the presence of water in the solar/supersolar regime and possible traces of AlO and TiH in the atmosphere of WASP-17 b. The atmosphere of the inflated hot Jupiter appears to be free from both an optically thick layer of gray clouds and hazes. Given the incompleteness of the STIS light curves, we reckon that additional HST/STIS observations will help to improve our knowledge about the limb of this gas giant. In fact, the remarkably large scale height of WASP-17 b makes the planet a perfect target for further atmospheric characterization, both from the ground and by current and next-generation space-based observatories such as the James Webb Space Telescope (Greene et al. 2016) and Ariel (Tinetti et al. 2018).

Software: Iraclis (Tsiaras et al. 2016a), TauREx 3 (Al-Refaie et al. 2021), PyLightcurve (Tsiaras et al. 2016b), Lightkurve (Lightkurve Collaboration et al. 2018), ExoTETHyS (Morello et al. 2020), Astropy (Price-Whelan et al. 2018), h5py (Collette 2013), emcee (Foreman-Mackey et al. 2013), Matplotlib (Hunter 2007), Multinest (Feroz et al. 2009), PyMultinest (Buchner et al. 2014), Pandas (McKinney & Pandas Development Team 2011), Numpy (Oliphant 2006), SciPy (Virtanen et al. 2020), corner (Foreman-Mackey 2016).

Appendix A
Spectral Data

The transit depth and associated errors for the STIS, WFC3 and IRAC data sets are shown in Tables 4, 5, and 6, respectively.

Table 4
Reduced and Fitted Spectral Data from the Raw HST/STIS Transmission Data Using Iraclis

Wavelength (μm)	Transit Depth (%)	Error (%)	Bandwidth (μm)	Instrument	Grating
0.385	1.593	0.045	0.050	HST STIS	G430L
0.420	1.529	0.030	0.020	HST STIS	G430L
0.440	1.525	0.037	0.020	HST STIS	G430L
0.460	1.537	0.028	0.020	HST STIS	G430L
0.480	1.484	0.027	0.020	HST STIS	G430L
0.500	1.473	0.029	0.020	HST STIS	G430L
0.520	1.525	0.027	0.020	HST STIS	G430L
0.540	1.534	0.036	0.020	HST STIS	G430L
0.560	1.472	0.041	0.020	HST STIS	G430L
0.385	1.391	0.032	0.050	HST STIS	G430L
0.420	1.444	0.046	0.020	HST STIS	G430L
0.440	1.417	0.028	0.020	HST STIS	G430L
0.460	1.407	0.026	0.020	HST STIS	G430L
0.480	1.400	0.027	0.020	HST STIS	G430L
0.500	1.431	0.026	0.020	HST STIS	G430L
0.520	1.444	0.027	0.020	HST STIS	G430L
0.540	1.466	0.033	0.020	HST STIS	G430L
0.560	1.486	0.037	0.020	HST STIS	G430L
0.570	1.479	0.021	0.040	HST STIS	G750L
0.605	1.456	0.036	0.030	HST STIS	G750L
0.635	1.464	0.034	0.030	HST STIS	G750L
0.665	1.440	0.027	0.030	HST STIS	G750L
0.700	1.488	0.022	0.040	HST STIS	G750L
0.760	1.497	0.033	0.080	HST STIS	G750L
0.870	1.394	0.031	0.140	HST STIS	G750L

Table 5
Reduced and Fitted Spectral Data from the Raw HST/WFC3 Transmission Data Using Iraclis

Wavelength (μm)	Transit Depth (%)	Error (%)	Bandwidth (μm)	Instrument	Grism
0.813	1.506	0.019	0.025	HST WFC3	G102
0.838	1.492	0.012	0.025	HST WFC3	G102
0.863	1.483	0.009	0.025	HST WFC3	G102
0.888	1.479	0.011	0.025	HST WFC3	G102
0.913	1.459	0.007	0.025	HST WFC3	G102
0.938	1.504	0.009	0.025	HST WFC3	G102
0.963	1.502	0.010	0.025	HST WFC3	G102
0.988	1.497	0.012	0.025	HST WFC3	G102
1.013	1.484	0.009	0.025	HST WFC3	G102
1.038	1.474	0.009	0.025	HST WFC3	G102
1.063	1.474	0.008	0.025	HST WFC3	G102
1.088	1.480	0.010	0.025	HST WFC3	G102
1.113	1.493	0.009	0.025	HST WFC3	G102
1.138	1.471	0.020	0.025	HST WFC3	G102
1.126	1.519	0.011	0.022	HST WFC3	G141
1.148	1.507	0.012	0.021	HST WFC3	G141
1.169	1.491	0.011	0.021	HST WFC3	G141
1.189	1.488	0.009	0.020	HST WFC3	G141
1.208	1.489	0.011	0.019	HST WFC3	G141
1.228	1.500	0.008	0.019	HST WFC3	G141
1.246	1.476	0.009	0.019	HST WFC3	G141
1.266	1.469	0.011	0.019	HST WFC3	G141
1.285	1.457	0.013	0.019	HST WFC3	G141
1.304	1.503	0.010	0.019	HST WFC3	G141
1.323	1.497	0.009	0.019	HST WFC3	G141
1.341	1.514	0.010	0.019	HST WFC3	G141
1.361	1.537	0.014	0.019	HST WFC3	G141
1.380	1.522	0.012	0.020	HST WFC3	G141
1.400	1.516	0.011	0.020	HST WFC3	G141
1.420	1.517	0.011	0.020	HST WFC3	G141
1.441	1.518	0.011	0.021	HST WFC3	G141
1.462	1.527	0.012	0.021	HST WFC3	G141
1.483	1.526	0.009	0.022	HST WFC3	G141
1.505	1.493	0.011	0.022	HST WFC3	G141
1.528	1.500	0.009	0.023	HST WFC3	G141
1.552	1.488	0.011	0.024	HST WFC3	G141
1.576	1.463	0.010	0.025	HST WFC3	G141
1.602	1.459	0.011	0.026	HST WFC3	G141
1.629	1.436	0.010	0.028	HST WFC3	G141

Table 6
Reduced and Fitted Spectral Data from the Raw Spitzer/IRAC Transmission Data Using TLCD-LSTM

Wavelength (μm)	Transit Depth (%)	Error (%)	Bandwidth (μm)	Instrument
3.560	1.500	0.032	0.380	Spitzer IRAC
4.500	1.521	0.018	0.560	Spitzer IRAC

Appendix B
Network Parameters

Table 7 shows the LSTM parameters used for detrending IRAC observations.

Table 7
Table of Parameters Used for Detrending IRAC Observations of WASP-17 b

|	IRAC Channel 1	IRAC Channel 2
Program	90092	90092
Aorkey	47040000	47039488
Radius (pixels)	3.25	3.25
Centroiding method	2D Gaussian	2D Gaussian
Start of test set (BMJD TDB)	56,422.595	56,426.330
End of test set (BMJD TDB)	56,422.783	56,426.518
No. layers	2	2
No. units	512	512
Dropout rate	10%	10%
Adam learning rate	0.005	0.005
β decay rate	0.95	0.95

Appendix C
Retrieval Contribution Functions

Case 1 (Figure 10) and Case 2 (Figure 11) spectra fitted by the best-fit model when accounting for an active and a homogenous star, respectively. The plots show the best-fit model (in black) and the contribution of CIA, active trace gases, clouds, and hazes to the final model.
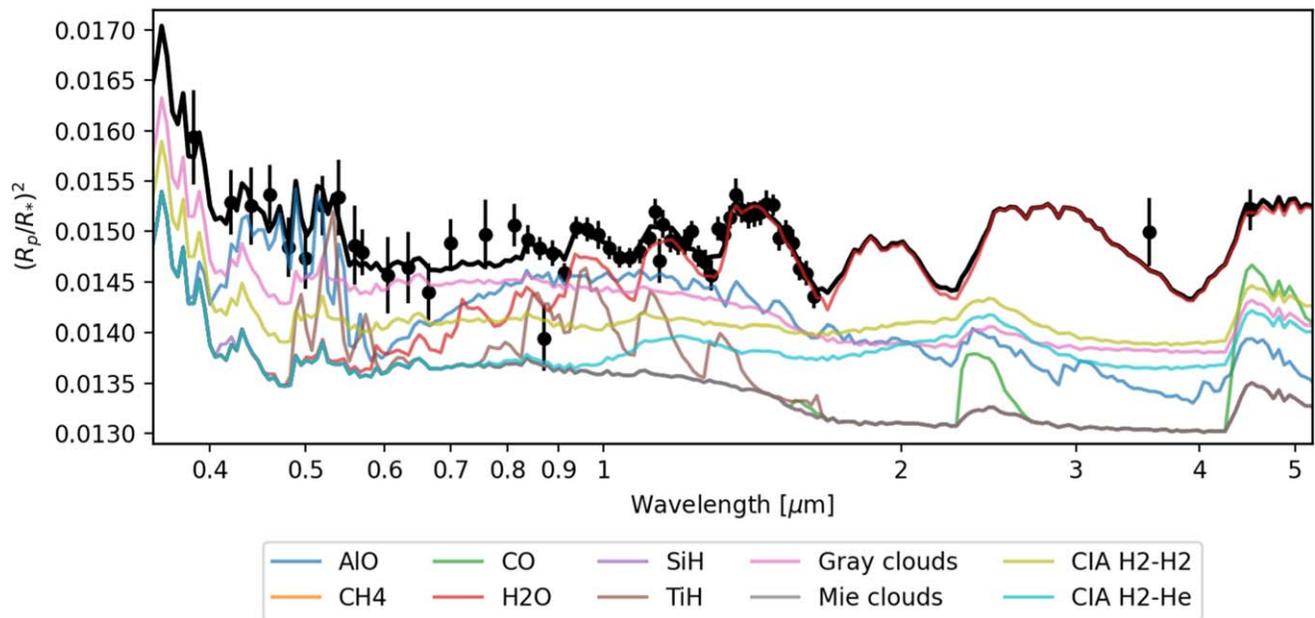
Figure 10. STIS visit 1&3, WFC3, and Spitzer data (Case 1) fitted by the best-fit model (black line) that includes an active star together with the contributions from CIA, active trace gases, clouds, and hazes. Stellar activity induces wavelength variations at the base of the model, which is why the gray cloud and Mie cloud contributions are not flat at the bottom.
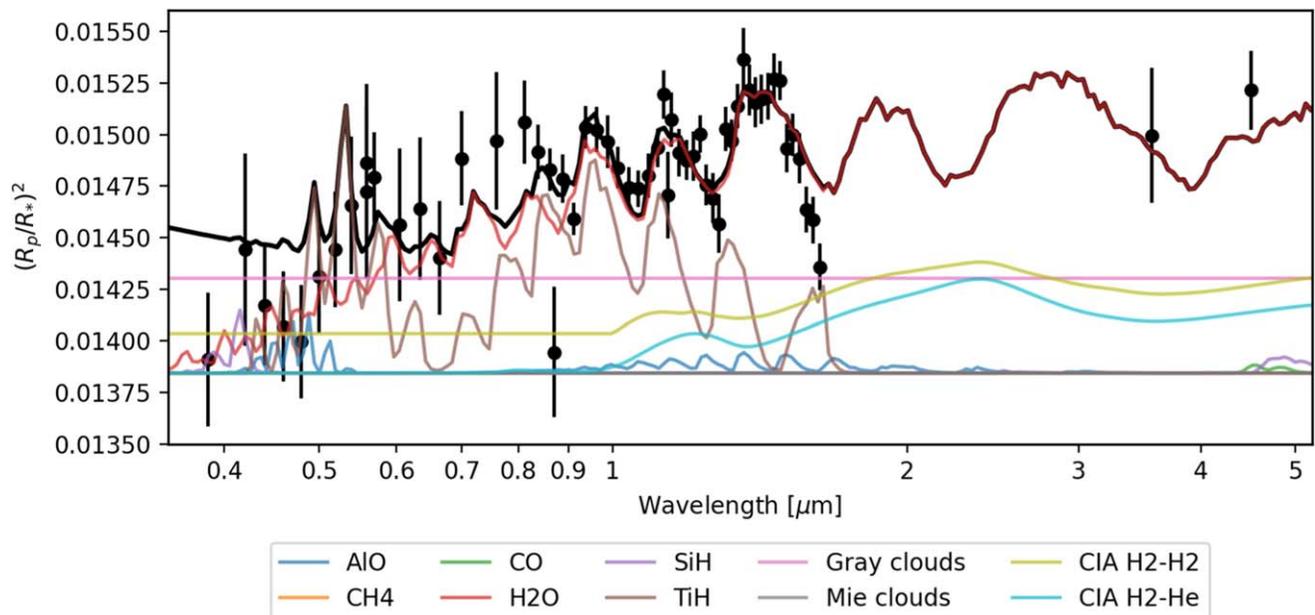
Figure 11. STIS visit 2&3, WFC3, and Spitzer data (Case 2) fitted by the best-fit model (black line) that includes a homogeneous star together with the contributions from CIA, active trace gases, clouds, and hazes.

ORCID iDs

Arianna Saba ⓘ https://orcid.org/0000-0002-1437-4228
Angelos Tsiaras ⓘ https://orcid.org/0000-0003-3840-1793
Mario Morvan ⓘ https://orcid.org/0000-0001-8587-2112
Alexandra Thompson ⓘ https://orcid.org/0000-0003-4128-2270
Quentin Changeat ⓘ https://orcid.org/0000-0001-6516-4493
Billy Edwards ⓘ https://orcid.org/0000-0002-5494-3237
Andrew Jolly ⓘ https://orcid.org/0000-0002-5888-4879
Ingo Waldmann ⓘ https://orcid.org/0000-0002-4205-5267
Giovanna Tinetti ⓘ https://orcid.org/0000-0001-6058-6654

References

Abel, M., Frommhold, L., Li, X., & Hunt, K. L. C. 2011, JPCA, 115, 6805
Abel, M., Frommhold, L., Li, X., & Hunt, K. L. C. 2012, JChPh, 136, 044319
Al-Refaie, A. F., Changeat, Q., Waldmann, I. P., & Tinetti, G. 2021, ApJ, 917, 37
Alderson, L., Wakeford, H., MacDonald, R., et al. 2022, MNRAS, 512, 4185
Allard, F., Homeier, D., Freytag, B., Schaffenberger, W., & Rajpurohit, A. 2013, MSAIS, 24, 128
Allard, N., Spiegelman, F., Leininger, T., & Molliere, P. 2019, A&A, 628, A120
Anderson, D., Smith, A., Lanotte, A., et al. 2011, MNRAS, 416, 2108
Anderson, D. R., Hellier, C., Gillon, M., et al. 2010, ApJ, 709, 159
Anisman, L. O., Edwards, B., Changeat, Q., et al. 2020, AJ, 160, 233
Arcangeli, J., Désert, J.-M., Parmentier, V., et al. 2019, A&A, 625, A136
Barstow, J. K., Aigrain, S., Irwin, P. G., & Sing, D. K. 2016, ApJ, 834, 50
Bate, M., Lodato, G., & Pringle, J. 2010, MNRAS, 401, 1505
Bayliss, D. D. R., Winn, J. N., Mardling, R. A., & Sackett, P. D. 2010, ApJL, 722, L224
Bento, J., Wheatley, P., Copperwheat, C., et al. 2014, MNRAS, 437, 1511
Bostroem, K., & Proffitt, C. 2011, STIS Data Handbook (Baltimore, MD: STScI)
Bourrier, V., Lovis, C., Beust, H., et al. 2018, Natur, 553, 477
Buchner, J., Georgakakis, A., Nandra, K., et al. 2014, A&A, 564, A125
Caldas, A., Leconte, J., Selsis, F., et al. 2019, A&A, 623, A161
Carone, L., Mollière, P., Zhou, Y., et al. 2021, A&A, 646, A168
Changeat, Q., Al-Refaie, A. F., Edwards, B., Waldmann, I. P., & Tinetti, G. 2021, ApJ, 913, 73
Changeat, Q., Edwards, B., Al-Refaie, A. F., et al. 2020, AJ, 160, 260
Charnay, B., Blain, D., Bézard, B., et al. 2021, A&A, 646, A171
Cho, J. Y., Menou, K., Hansen, B. M., & Seager, S. 2003, ApJL, 587, L117
Cho, J. Y., Skinner, J. W., & Thrastarson, H. T. 2021, ApJL, 913, L32
Chubb, K. L., Rocchetto, M., Yurchenko, S. N., et al. 2021, A&A, 646, A21
Ciardi, D. R., Von Braun, K., Bryden, G., et al. 2011, AJ, 141, 108
Claret, A. 2000, A&A, 363, 1081
Coles, P. A., Yurchenko, S. N., & Tennyson, J. 2019, MNRAS, 490, 4638
Collette, A. 2013, Python and HDF5 (Sebastopol, CA: O'Reilly Media, Inc.)
Dulick, M., Bauschlicher, C., Jr, Burrows, A., et al. 2003, ApJ, 594, 651
Edwards, B., Changeat, Q., Baeyens, R., et al. 2020a, AJ, 160, 8
Edwards, B., Changeat, Q., Mori, M., et al. 2020b, AJ, 161, 44
Feng, Y. K., Line, M. R., & Fortney, J. J. 2020, AJ, 160, 137
Feroz, F., Hobson, M., & Bridges, M. 2009, MNRAS, 398, 1601
Fletcher, L. N., Gustafsson, M., & Orton, G. S. 2018, ApJS, 235, 24
Fleury, B., Gudipati, M. S., Henderson, B. L., & Swain, M. 2019, ApJ, 871, 158
Foreman-Mackey, D. 2016, JOSS, 1, 24
Foreman-Mackey, D., Hogg, D. W., Lang, D., & Goodman, J. 2013, PASP, 125, 306
Fortney, J. J., Lodders, K., Marley, M. S., & Freedman, R. S. 2008, ApJ, 678, 1419
Gharib-Nezhad, E., Iyer, A. R., Line, M. R., et al. 2021, ApJS, 254, 34
Gordon, I., Rothman, L. S., Wilzewski, J. S., et al. 2016, AAS/Division for Planetary Sciences Meeting Abstracts, 48, 421.13
Goyal, J. M., Mayne, N., Drummond, B., et al. 2020, MNRAS, 498, 4680
Greene, T. P., Line, M. R., Montero, C., et al. 2016, ApJ, 817, 17
Guilluy, G., Gressier, A., Wright, S., et al. 2020, AJ, 161, 19
Guo, X., Crossfield, I. J., Dragomir, D., et al. 2020, AJ, 159, 239
Hébrard, G., Ehrenreich, D., Bouchy, F., et al. 2011, A&A, 527, L11
Hochreiter, S., & Schmidhuber, J. 1997, Neural Comput., 9, 1735
Hunter, J. D. 2007, CSE, 9, 90
Husser, T.-O., Wende-von Berg, S., Dreizler, S., et al. 2013, A&A, 553, A6

Ida, S., & Lin, D. 2004, ApJ, 616, 567
Irwin, P. G., Parmentier, V., Taylor, J., et al. 2020, MNRAS, 493, 106
Jenkins, J. M., Twicken, J. D., McCauliff, S., et al. 2016, Proc. SPIE, 9913, 99133E
Johnson, J. A., Winn, J. N., Albrecht, S., et al. 2009, PASP, 121, 1104
Kawashima, Y., & Ikoma, M. 2018, ApJ, 853, 7
Khalafinejad, S., Salz, M., Cubillos, P. E., et al. 2018, A&A, 618, A98
Knutson, H. A., Lewis, N., Fortney, J. J., et al. 2012, ApJ, 754, 22
Kokori, A., Tsiaras, A., Edwards, B., et al. 2021, ExA, Online First
Kramida, A. 2013, Fusion Sci. Technol., 63, 313
Kreidberg, L., Line, M. R., Parmentier, V., et al. 2018, AJ, 156, 17
Lee, J.-M., Heng, K., & Irwin, P. G. 2013, ApJ, 778, 97
Li, G., Gordon, I. E., Rothman, L. S., et al. 2015, ApJS, 216, 15
Lightkurve Collaboration, Cardoso, J. V. d. M., Hedges, C., et al. 2018, Lightkurve: Kepler and TESS time series analysis in Python, Astrophysics Source Code Library, ascl:1812.013
Lin, D. N., Bodenheimer, P., & Richardson, D. C. 1996, Natur, 380, 606
MacDonald, R. J., Goyal, J. M., & Lewis, N. K. 2020, ApJL, 893, L43
Mamajek, E. E., & Hillenbrand, L. A. 2008, ApJ, 687, 1264
Mandell, A. M., Haynes, K., Sinukoff, E., et al. 2013, ApJ, 779, 128
McKemmish, L. K., Masseron, T., Hoeijmakers, H. J., et al. 2019, MNRAS, 488, 2836
McKemmish, L. K., Yurchenko, S. N., & Tennyson, J. 2016, MNRAS, 463, 771
McKinney, W. & Pandas Development Team 2011, pandas: powerful Python data analysis toolkit, Release 1.4.2, https://pandas.pydata.org/docs/pandas.pdf
McQuillan, A., Mazeh, T., & Aigrain, S. 2014, ApJS, 211, 24
Mikal-Evans, T., Sing, D. K., Goyal, J. M., et al. 2019, MNRAS, 488, 2222
Morello, G., Claret, A., Martin-Lagarde, M., et al. 2020, AJ, 159, 75
Morvan, M., Nikolaou, N., Tsiaras, A., & Waldmann, I. P. 2020, AJ, 159, 109
Mugnai, L. V., Modirrousta-Galian, D., Edwards, B., et al. 2021, AJ, 161, 284
Nagasawa, M., Ida, S., & Bessho, T. 2008, ApJ, 678, 498
Norris, C. M., Beeck, B., Unruh, Y. C., et al. 2017, A&A, 605, A45
Oliphant, T. E. 2006, A guide to NumPy, Vol. 1 (Trelgol Publishing USA)
Patrascu, A. T., Yurchenko, S. N., & Tennyson, J. 2015, MNRAS, 449, 3613
Peek, J. E., Desai, V., White, R. L., et al. 2019, arXiv:1907.06234
Pinhas, A., Madhusudhan, N., Gandhi, S., & MacDonald, R. 2018, MNRAS, 482, 1485
Pluriel, W., Whiteford, N., Edwards, B., et al. 2020a, AJ, 160, 112
Pluriel, W., Zingales, T., Leconte, J., & Parmentier, V. 2020b, arXiv:2003.05943
Polyansky, O. L., Kyuberis, A. A., Zobov, N. F., et al. 2018, MNRAS, 480, 2597
Price-Whelan, A. M., Sipőcz, B., Günther, H., et al. 2018, AJ, 156, 123
Prichard, L., Welty, D., & Jones, A. 2022, STIS Instrument Handbook for Cycle 30, Vol. 21 (Baltimore, MD: STSci), 21
Rackham, B., Espinoza, N., Apai, D., et al. 2017, ApJ, 834, 151
Rackham, B. V., Apai, D., & Giampapa, M. S. 2018, ApJ, 853, 122
Rackham, B. V., Apai, D., & Giampapa, M. S. 2019, AJ, 157, 96
Ricker, G. R., Winn, J. N., Vanderspek, R., et al. 2014, JATIS, 1, 014003
Robinson, T. D., & Catling, D. C. 2014, NatGe, 7, 12
Rothman, L. S., Gamache, R. R., Goldman, A., et al. 1987, ApOpt, 26, 4058
Rothman, L. S., & Gordon, I. E. 2014, in 13th International HITRAN Conf. 49
Rothman, L. S., Gordon, I., Barber, R., et al. 2010, JQSRT, 111, 2139
Sedaghati, E., Boffin, H. M. J., Jeřabková, T., et al. 2016, A&A, 596, A47
Sharp, C. M., & Burrows, A. 2007, ApJS, 168, 140
Shulyak, D., Lara, L. M., Rengel, M., & Nèmec, N.-E. 2020, A&A, 639, A48
Simpson, E., Pollacco, D., Cameron, A. C., et al. 2011, MNRAS, 414, 3023
Sing, D. K., Fortney, J. J., Nikolov, N., et al. 2016, Natur, 529, 59
Skaf, N., Bieger, M. F., Edwards, B., et al. 2020, AJ, 160, 109
Southworth, J., Hinse, T. C., Dominik, M., et al. 2012, MNRAS, 426, 1338
Stevenson, K. B., Line, M. R., Bean, J. L., et al. 2017, AJ, 153, 68
Tennyson, J., Yurchenko, S. N., Al-Refaie, A. F., et al. 2016, JMoSp, 327, 73
Tinetti, G., Drossart, P., Eccleston, P., et al. 2018, ExA, 46, 135
Triaud, A. H., Cameron, A. C., Queloz, D., et al. 2010, A&A, 524, A25
Tsiaras, A., Rocchetto, M., Waldmann, I., et al. 2016a, AJ, 820, 99
Tsiaras, A., Waldmann, I., Rocchetto, M., et al. 2016b, ApJ, 832, 202
Tsiaras, A., Waldmann, I. P., Tinetti, G., Tennyson, J., & Yurchenko, S. N. 2019, NatAs, 3, 1086
Tsiaras, A., Waldmann, I., Zingales, T., et al. 2018, AJ, 155, 156
Venot, O., & Agúndez, M. 2015, ExA, 40, 469
Venot, O., Hébrard, E., Agúndez, M., Decin, L., & Bounaceur, R. 2015, A&A, 577, A33

Venot, O., Hébrard, E., Agúndez, M., et al. 2012, A&A, 546, A43

Virtanen, P., Gommers, R., Oliphant, T. E., et al. 2020, Nature methods, 17, 261

Wende, S., Reiners, A., Seifahrt, A., & Bernath, P. 2010, A&A, 523, A58

Winn, J. N., Johnson, J. A., Fabrycky, D., et al. 2009, ApJ, 700, 302

Woitke, P., Helling, C., Hunter, G., et al. 2018, A&A, 614, A1

Wood, P. L., Maxted, P. F. L., Smalley, B., & Iro, N. 2011, MNRAS, 412, 2376

Yip, K. H., Changeat, Q., Edwards, B., et al. 2020, AJ, 161, 4

Yurchenko, S. N., Sinden, F., Lodi, L., et al. 2018, MNRAS, 473, 5324

Yurchenko, S. N., & Tennyson, J. 2014, MNRAS, 440, 1649

Zhou, G., & Bayliss, D. D. R. 2012, MNRAS, 426, 2483